Ab initio energetics of LaBO_3(001) (B=Mn, Fe, Co, and Ni) for solid oxide fuel cell cathodes

Yueh-Lin Lee,[1] Jesper Kleis,[2] Jan Rossmeisl,[2] and Dane Morgan[1,3]
[1]*Materials Science Program, University of Wisconsin–Madison, Madison, Wisconsin 53706, USA*
[2]*Center for Atomic-Scale Materials Design (CAMD), Department of Physics, Technical University of Denmark, Building 307, DK-2800 Lyngby, Denmark*
[3]*Department of Materials Science and Engineering, University of Wisconsin–Madison, Madison, Wisconsin 53706, USA*
(Received 26 April 2009; revised manuscript received 29 October 2009; published 1 December 2009)

LaBO_3 (B=Mn, Fe, Co, and Ni) perovskites form a family of materials of significant interest for cathodes of solid oxide fuel cells (SOFCs). In this paper *ab initio* methods are used to study both bulk and surface properties of relevance for SOFCs, including vacancy formation and oxygen binding energies. A thermodynamic approach and the density functional theory plus U method are combined to obtain energies relevant for SOFC conditions ($T \approx 800$ °C, $PO_2 \approx 0.2$ atm). The impact of varying U_{eff} ($U_{\text{eff}}=U-J$) on energy and electronic structure is explored in detail and it is shown that optimal U_{eff} values yield significantly better agreement with experimental energies than $U_{\text{eff}}=0$ (which corresponds to the standard generalized gradient approximation). LaBO_3 oxygen vacancy formation energies are predicted to be in the order Fe > Mn > Co > Ni (where the largest implies most difficult to form a vacancy). It is shown that (001) BO_2 terminated surfaces have 1–2 eV lower vacancy formation energies and therefore far higher vacancy concentrations than the bulk. The stable surface species at low temperature are predicted to be the superoxide O_2^- for B=Mn, Fe, Co and a peroxide O_2^{2-} with a surface oxygen for B=Ni. Entropy effects are predicted to stabilize the monomer oxygen surface state for all B cations at higher temperatures. Overall oxygen coverage of the (001) BO_2 surface is predicted to be quite low at SOFC operating conditions. These results will aid in understanding the oxygen reduction reaction on perovskite SOFC cathodes.

DOI: 10.1103/PhysRevB.80.224101 PACS number(s): 82.47.Ed, 82.20.Wt, 31.15.es, 68.47.Gh

I. INTRODUCTION

The perovskite type lanthanum strontium transition metal oxides (La,Sr)BO_3 (B=Mn, Fe, Co, and Ni) and closely related alloys are frequently explored as the cathode materials for solid oxide fuel cells (SOFCs). Their utility in SOFCs derives from their ability to catalyze the oxygen reduction reaction (ORR), as well as their low cost, high-temperature stability, and acceptable thermal expansion properties.[1,2] Essential to the use of LaBO_3 compounds in SOFCs is the efficiency of the ORR, which occurs on the LaBO_3 material's surface during SOFC operation. The ORR contributes a significant part of the electrode overpotential loss by activation polarization.[2] The ORR contribution to overpotential is likely to become increasingly important as other sources of voltage loss are reduced (e.g., by the making thinner and less resistive electrolyte films) and as researchers push to lower the SOFC operating temperatures to reduce degradation rates and material costs. Due to the complexity of the ORR mechanisms and the difficulty of resolving surface ORR steps in experiments, factors governing the cathode performances are still poorly understood, including the rate-limiting steps and how different transition metal cations alter the catalytic properties.

Ab initio methods offer a powerful tool to investigate the ORR on complex oxides. The local density approximation (LDA) or the generalized gradient approximation (GGA) to density functional theory (DFT) has been widely used in probing catalytic properties by investigating electronic structures, reaction energetics, and activation barriers at molecular scales. DFT approaches have been successfully applied in understanding trends in reactivity for metals.[3] However, DFT with LDA or GGA is known to fail to obtain correct electronic structure for strongly correlated systems due to errors associated with the on-site Coulomb and exchange interactions.[4] These errors limit DFT's applicability in late transition metal oxides and rare-earth compounds.[5] A well-known simple but successful approach to improve the accuracy of DFT for the strongly correlated electronic systems is the so-called LDA/GGA+U (or just DFT+U) method, in which a Hubbard-model-type correction is added to account for the on-site Coulomb interactions in the localized d or f orbitals.[4,6] Although extensive DFT+U studies[7–14] have been carried out to understand the LaBO_3 (B=Mn, Fe, Co, and Ni) electronic and magnetic structures, to our knowledge, none has focused on the surface properties related to catalysis in these systems. A few *ab initio* studies[15–18] have used just LDA/GGA to investigate the surface ORR energetics for SOFC applications and proposed possible ORR mechanisms based on the calculated reaction energetics. However, it is important to consider LaBO_3 materials using the more accurate DFT+U approaches, as LDA/GGA can produce significant errors in these systems.[5] A good example demonstrating the need for DFT+U approaches can be found in the CO/NiO and NO/NiO adsorption energetics.[19,20] For both these systems the DFT+U approach correctly predicts the adsorption energy and the unusual tilted adsorption geometry, whereas both DFT and Hartree-Fock based quantum chemical approaches fail to do so.

In this paper we investigate oxygen defect and binding energetics as a function of cation in LaBO_3 (B=Mn, Fe, Co, and Ni) perovskites and discuss implications for the ORR. We have chosen to focus on the (001) B-terminated surface. This surface is chosen because the (001) surfaces are generally the most stable in perovskites[16,17] and it is reasonable to

expect that catalytic activity may involve interaction with the redox active transition metals. The MnO_2 termination has been predicted to be the most stable termination for (001) $LaMnO_3$, although Sr doping may stabilize the (La,Sr)O surface.[21] The most active surface for ORR under SOFC conditions in ABO_3 perovskites is still not known although a few studies have now suggested AO termination may play role.[22,23] Some care is necessary to accurately study the behavior of oxygen defects and surface species,[5,24] especially under SOFC conditions, which need to include effects of high temperatures (e.g., up to 1000 °C) and a wide range of oxygen partial pressures (PO_2). We propose a simple but systematic approach which includes a correction for the O_2 overbinding error in DFT with LDA/GGA,[25] essential oxygen gas thermodynamics at high-temperature using experimentally derived expressions, approximate vibrational contributions from the solid phase oxygen, appropriate treatment of Jahn-Teller distortions for SOFC conditions, and corrections for correlated electron effects using GGA+U. The approach takes into account and allows us to obtain nonconfigurational reaction free energies [which are true reaction free energies minus the configurational (entropic) contribution] for oxygen defects and surface species as a function of temperature and oxygen partial pressure. While all the approaches taken here involve many limitations we have tried to include at least approximate treatment of physics that contributes more than ±0.2 eV to the defect and surface binding energetics. Thus, ±0.2 eV is a qualitative target accuracy for the calculations, although the accumulated errors, unavoidable approximations, and differences between idealized and real systems are likely to create larger total uncertainties when comparing to experiments.

This paper is arranged as follows. Section II contains the calculation details, including details of the O_2 thermodynamics and convergence testing. Section III contains the energetics of oxygen vacancies and adsorption at the (001) surface of $LaBO_3$ for a range of U values and transition metal types. Section III also contains a discussion of the implications of these energetics for the ORR on these materials. Section IV contains a summary.

II. CALCULATION DETAILS

A. DFT calculation methods

Spin polarized DFT calculations were performed with the Vienna Ab-initio Simulation Package (VASP)[26] using a plane-wave basis set, the GGA-Perdew-Wang-91 (PW91)[27] exchange-correlation function, and the projector augmented wave (PAW) method.[28] We used PAW potentials with electronic configurations La ($5s2$ $5p6$ $6s2$ $5d1$), O_s (soft oxygen potential, $2s2$ $2p4$), B=Mn_{pv} ($3p6$ $3d6$ $4s1$), Fe_{pv} ($3p6$ $3d7$ $4s1$), Co ($3d8$ $4s1$), and Ni_{pv} ($3p6$ $3d9$ $4s1$). All calculations were done with an energy cutoff of 600 eV. A $2\times2\times2$ Monkhorst-Pack k-point mesh[29] in the Brillouin zone was used for a $2\times2\times2$ supercell of the primitive perovskite formula unit (containing 40 total atoms) and the k-point density in reciprocal space was kept as close to this value as possible for different slab calculations. The surface calculations were done with an eight-layer slab with a $2\times2\times1$ k-point mesh. The energies were converged to within ~3 meV per atom with respect to the k points and energy cutoff. Structural relaxations were converged to within 1 meV per atom.

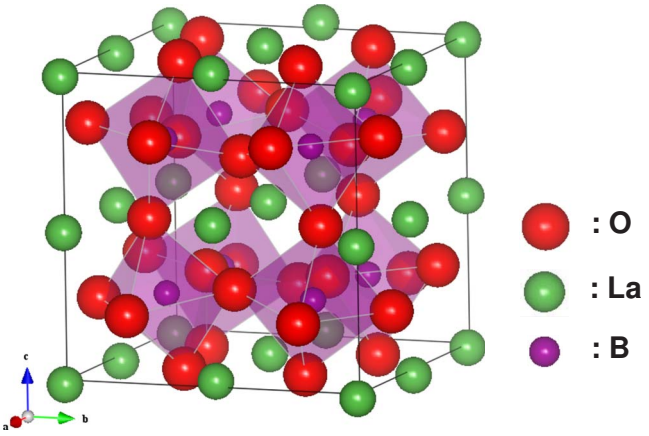

FIG. 1. (Color online) An internally relaxed $LaBO_3$ (B=Mn, Fe, Co, and Ni) $2\times2\times2$ bulk structure with the lattice constant fixed to that of a fully relaxed ideal cubic perovskite. This structure is used to approximate the $LaBO_3$ perovskites under SOFC condition.

In our GGA+U calculations, we adopted the rotationally invariant GGA+U approach[30] in the simplified spherically averaged version,[31] where the parameters U and J do not enter into the density functional separately but instead as a combined effective interaction parameter, $U_{eff}=U-J$. The calculated energies were therefore insensitive to the J parameter at fixed U_{eff} and we used J=1 eV in all GGA+U calculations.

The optimal choice of relaxations is somewhat unclear for SOFC studies. Full relaxation frequently leads to large Jahn-Teller (J-T) distortions, which can alter the structure, energetics, and electronic structure significantly. However, the high-temperature structures, appropriate for SOFC conditions (700–1200 K), typically exhibit an averaged cubic symmetry, which is consistent with no average Jahn-Teller distortion. The cubic symmetry is a result of the fact that the SOFC operating temperatures (700–1200 K) are generally higher than the cooperative J-T orbital order/disorder transition temperature for the J-T distorted systems[32,33] (T_{JT} =750 K for $LaMnO_3$ and T_{JT}=500 K for $LaCoO_3$). Although the high-temperature material is on average cubic, it is likely that disordered local J-T distortion persists.[34] We have therefore attempted to perform calculations consistent with overall cubic symmetry constraints but also allowing for local distortions inside the supercell. For bulk studies, ideal cubic perovskite unit cells with no internal relaxation ($LaBO_3$) are first relaxed to obtain lattice constants. Bulk calculations are then performed in a $2\times2\times2$ cubic supercell, in which ions are relaxed internally to restore BO_6 octahedron distortion ($GdFeO_3$ type rotation), as shown in Fig. 1. It is noted that the constraint of retaining cubic lattice parameters in a $2\times2\times2$ cell completely suppresses the Jahn-Teller distortions in the undefected bulk, which is likely to create an artificially high destabilization of the bulk enthalpy. However, the relaxations do allow for local distortions associated with the Jahn-Teller effect to occur when

defects are introduced, e.g., by a vacancy. The Jahn-Teller distortions are typically less than 0.3 eV/Jahn-Teller ion.[35] Specifically, our calculation results suggest that the fully relaxed $2\times2\times2$ $LaMnO_3$ and $LaCoO_3$ perovskites are about 0.05 eV/Jahn-Teller ion more stable than the constrained $2\times2\times2$ cubic supercells. Therefore, we expect our approximate treatment of Jahn-Teller effects will introduce only small percentage errors in the *ab initio* defect energetics. The slab calculations for surfaces, discussed further below, are performed with lattice parameter a and b identical to those from the bulk cubic cell, although they are allowed to relax freely in the c direction.

The magnetic structures of LaBO_3 are quite complex and undergo phase transitions at elevated temperatures. The experimental LaBO_3 ground state magnetic phases at room temperature[8] are $LaMnO_3 \rightarrow A$-type antiferromagnetic (AAFM), $LaFeO_3 \rightarrow G$-type antiferromagnetic (GAFM), $LaCoO_3 \rightarrow$ nonmagnetic (low spin state), and $LaNiO_3 \rightarrow$ paramagnetic. Under solid oxide fuel cell conditions ($T=800-1300$ K), $LaMnO_3$, $LaFeO_3$, $LaCoO_3$, and $LaNiO_3$ all become paramagnetic.[32,36,37] In order to use a consistent and tractable set of magnetic structures we apply the ferromagnetic (FM) state for all the studies. In addition, the ground state antiferromagnetic structures for $LaMnO_3$ (AAFM) and $LaFeO_3$ (GAFM) are also used to investigate how key defect energies might change with the experimental low-temperature magnetic ordering. For $LaCoO_3$ and $LaNiO_3$, we expect that the energy differences between different magnetic structures (typically of the scale of $10^{-1}-10^{-2}$ eV/magnetic atom) are relatively small as compared to the defect and surface binding energies being studied (typically $10^{0}-10^{-1}$ eV per defect or surface binding atom). Therefore, we believe that the choice of ferromagnetic structures does not qualitatively alter the energetic trends discussed in this paper.

B. O_2 correction and U_{eff} fitting

Wang *et al.*[25] carried out a systematic GGA+U study on redox energetics of transition metal oxides and proposed that errors in DFT redox energetics come from two parts: (1) error from calculating the O_2 molecule in DFT with LDA/GGA and (2) self-interaction (on-site interaction) error in solids with LDA/GGA. Work on Li intercalation reactions from Zhou *et al.*[38] has also demonstrated that self-interaction errors are very significant when calculating redox energies in traditional LDA and GGA approaches. Both O_2 and self-interaction errors must be corrected in the present studies.

First we consider the correction for calculated errors in O_2. By fitting experimental formation enthalpy and calculated oxide formation energies (e.g., $M+\frac{x}{2}O_2 \Rightarrow MO_x$), Wang *et al.* obtained $\Delta h^0_{O_2}=1.36$ eV/O_2 as a correction (destabilization) of the *ab initio* calculated O_2 energy. Because of the way it is fit, the $\Delta h^0_{O_2}$ actually contains a number of terms (not just a correction of O_2 overbinding), including correction for errors in the binding energy of O_2, correction for enthalpy contributions associated with going from the $T=0$ solid to the $T=T^0$ gas phase oxygen ($T^0=298$ K), and thermodynamic contributions to the enthalpy at T^0 from the solid phase oxygen. The consequence of applying the $\Delta h^0_{O_2}$ correction for redox reactions is to introduce a constant shift (in the opposite way for reduction and oxidation) on the calculated reduction and oxidation energies (stabilizing oxidation energies and destabilizing reduction energies). Note that the $\Delta h^0_{O_2}$ correction is potentially dependent on the specific choice of exchange-correlation approximation (e.g., LDA vs GGA) and pseudopotential. To obtain the $\Delta h^0_{O_2}$ term for our study (GGA-PW91 and O_s PAW potential), we follow the approach used by Wang *et al.*[25] and fit the formation enthalpies of several nontransition metal oxides,[39,40] as shown in Fig. 2, for both Perdew-Burke-Ernzerhof (PBE) (used in by Wang *et al.*) and PW91 GGA functionals. A summary of the O_2 energetics and corrections for the PBE (O) (400 eV PAW potential cutoff energy) and the PW91 (O_s) (250 eV PAW potential cutoff energy) along with the experimental oxygen binding energy[41] is shown in Table I. We find that the PBE (O) data have an O_2 energy correction $\Delta h^0_{O_2}=1.36$ eV, consistent with Wang *et al.*,[25] and PW91 (O_s) (used in this work) has an optimal O_2 energy correction $\Delta h^0_{O_2}=0.33$ eV. While the difference between the two $\Delta h^0_{O_2}$ is quite large (1.03 eV), the corrected O_2 total energies are much closer (0.25 eV/O_2) than the uncorrected O_2 total energies (0.77 eV/O_2). When compared to experimental values, the corrected O_2 binding energies, which are the O_2 energy referenced to the spin-polarized O atom, show errors of −0.43 eV/O_2 with PW91 (O_s) and +0.55 eV/O_2 with PBE (O). Because the fitting of the O_2 energy with the experimental oxide formation enthalpies involves electron interchange between solids and oxygen gas molecules, Wang *et al.*[25] suggested that the errors in the O_2 binding energy are associated with the error of adding electrons to the O $2p$ orbitals when O^{2-} is formed from O_2.

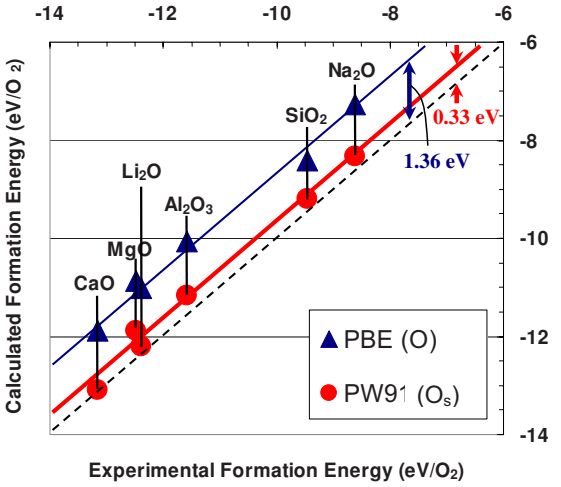

FIG. 2. (Color online) Formation energies (per O_2) of nontransition metal oxides (CaO, MgO, Li_2O, Al_2O_3, SiO_2, and Na_2O) with PBE (o) (cutoff energy of 400 eV) and PW91 (O_s) (cutoff energy of 250 eV) PAW potentials as a function of the experimental formation enthalpies extracted from Ref. 25. Each solid represents the best fit to each set of data. A 1.36 eV/O_2 (consistent with Ref. 25) and a 0.33 eV/O_2 energy correction are obtained for PBE (o) and PW91 (O_s), respectively. The 0.33 eV/O_2 correction to the O_2 energy is applied in this work.

TABLE I. Calculated O_2 total energies, O_2 binding energies (referenced to spin-polarized O atom), and corrections using different exchange-correlation functionals and PAW potentials. Corrections obtained from fits to experimental Na_2O, Li_2O, MgO, CaO, Al_2O_3, and SiO_2 formation enthalpies (experimental values from Refs. 39 and 40).

	This work (GGA-PW91, Os pp)	This work and Ref. 25 (GGA-PBE, O pp)
Calculated O_2 total energy	−9.09 eV/O_2	−9.86 eV/O_2
Calculated O_2 binding energy	−5.99 eV/O_2	−6.04 eV/O_2
O_2 correction (Δh^0_{O2})	0.33 eV/O_2	1.36 eV/O_2
Corrected O_2 total energy	−8.76 eV/O_2	−8.50 eV/O_2
Corrected O_2 binding energy	−5.66 eV/O_2	−4.68 eV/O_2
Experimental O_2 binding energy[a]	−5.23 eV/O_2	

[a]Reference 41.

Now we take into account the self-interaction errors that occur with traditional DFT with LDA/GGA. These will be treated with the GGA+U approach, but different choices for the U_{eff} value are possible. A general empirical selection of U_{eff} for the DFT+U method is to treat U_{eff} (or U and J) as a tunable parameter, which is chosen to fit known properties of the system of interest (e.g., band gap, optical spectroscopy, redox energetics, etc.). For example, in Ref. 25, the optimal U is determined by fitting enthalpies of oxidation reactions that oxidize a low-valent oxide to a higher-valent one (e.g., $MO_x+\frac{y-x}{2}O_2 \Rightarrow MO_y$). In this study, a wide range of U_{eff} values (from 0 to 6.4 eV) is investigated to understand the relationship between reaction energetics and U_{eff}. Then we apply the optimal U_{eff} from Ref. 25 (U_{eff}=4, 4, 3.3, and 6.4 eV for Mn, Fe, Co, and Ni, respectively) to obtain reaction energies for understanding the ORR energetics with respect to transition metal types. In general, we will refer to the set of U_{eff} values from Ref. 25 as the optimal U_{eff}.

To test the effect on the energetics of applying the optimal U_{eff} from binary BO_x transition metal oxides to LaBO_3, we compare the experimental formation reaction enthalpies[42,43] of $\frac{1}{2}La_2O_3+BO_x+\frac{1}{2}(\frac{3}{2}-x)O_2 \Rightarrow LaBO_3$ at 298 K to the calculated LaBO_3 formation energies. We used fully relaxed $2\times2\times2$ supercells with experimental ground state magnetic structures for $LaMnO_3$ (A-type antiferromagnetic) and $LaFeO_3$ (G-type antiferromagnetic) and the ferromagnetic structure for $LaCoO_3$ and $LaNiO_3$ as an approximation for calculating LaBO_3 total energies. The crystal structures used in the BO_x calculations follow Ref. 25 and that for La_2O_3 is taken from Ref. 44. The same U_{eff} is applied to the transition metal 3d orbitals in LaBO_3 and BO_x, and the 0.33 eV/O_2 correction is included as reactions are involved with O_2 gas.

As shown in Fig. 3, the use of optimal U_{eff} values gives a root-mean-square (rms) error of only 0.21 eV, significantly reduced from the pure GGA (U_{eff}=0 eV) rms value of 0.67 eV. This result demonstrates that the use of the optimal U_{eff} from Ref. 25 can significantly reduce the errors in the pure GGA LaBO_3 energy calculations. The value of using optimal U_{eff} is even clearer if we restrict the analysis to the reactions in Fig. 3 which include changes in transition metal valence (redox reactions), where U_{eff} is expected to have the most impact. For these cases the root-mean-square error for the pure GGA data is 0.78 eV and that of the optimal U_{eff} calculations is 0.16 eV. The significant improvement in LaBO_3 formation energies obtained using optimal U_{eff} from Ref. 25 supports the use of these U_{eff} values for LaBO_3 defect and surface species energy calculations.

C. Surface simulations and convergence vs slab thickness

Surface structures were calculated by truncating the bulk with insertion of 10 Å vacuum above the surface under periodic conditions. The (001) type surfaces are chosen to simulate the surface reactions in this work. The LaBO_3(001) surfaces are polar,[17,45] which could potentially cause problems with the accuracy of the calculations. To assess the magnitude of the effect and the possibility of applying the commonly used "symmetric slab" approach we have calculated the $LaMnO_3$ surface energies of 1×1 eight-layer asymmetric and 1×1 nine-layer symmetric slabs. The 1×1 eight-layer slab has a dipole moment and is stoichiometric, and its surface energy is defined as $\frac{1}{2}(E_{8L(1\times1)\_slab}-4E_{1\times1\times1\_bulk})$,

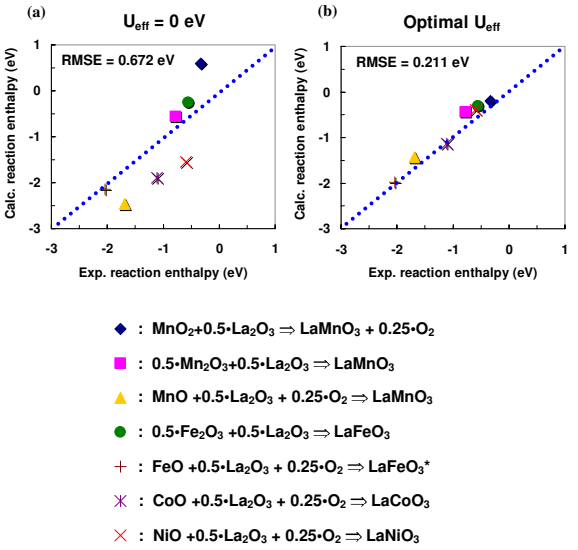

*This reaction enthalpy is obtained from adding the experimental oxidation enthalpy of $FeO+0.25\cdot O_2 \Rightarrow Fe_2O_3$ from Ref. 25 to that of the $0.5\cdot Fe_2O_3+0.5\cdot La_2O_3 \Rightarrow LaFeO_3$ from Ref. 43.

FIG. 3. (Color online) Calculated LaBO_3 (B=Mn, Fe, Co, and Ni) formation energies of $\frac{1}{2}La_2O_3+BO_x+\frac{1}{2}(\frac{3}{2}-x)O_2 \Rightarrow LaBO_3$ vs experimental formation reaction enthalpies (at 298 K) taken from Refs. 42 and 43 at (a) U_{eff}=0 eV and (b) optimal U_{eff}. The root mean square root error of the U_{eff}=0 eV data is 0.672 eV while that of those at optimal U_{eff} is 0.211 eV.

where $E_{8L(1\times1)\_slab}$ and $E_{1\times1\times1\_bulk}$ are the calculated VASP energies of a 1×1 eight-layer slab and a $1\times1\times1$ bulk, respectively. The 1×1 nine-layer symmetric slab does not have a dipole moment and is off stoichiometric, and its surface energy is defined as $\frac{1}{4}[(E_{9L(1\times1)\_slab\_LaO}+E_{9L(1\times1)\_slab\_MnO_2}-9E_{1\times1\times1\_bulk})]$, where $E_{9L(1\times1)\_slab\_LaO}$ and $E_{9L(1\times1)\_slab\_MnO_2}$ are the calculated energies of a LaO and a MnO_2 terminated 1×1 nine-layer slab, respectively. The surface energy difference between the two sets of calculations is insignificant (less than 0.05 eV/Mn) as compared to the scale of the reaction energetics (10^0–10^{-1} eV/O) in this work. On the other hand, we noticed that the nonstoichiometry of the 1×1 nine-layer slab, which impacts the average valence of *B* cations, has a significant influence on reaction energetics: a test on surface oxygen vacancy formation energies of 1×1 nine-layer symmetric (nonstoichiometric) and 1×1 eight-layer asymmetric (stoichiometric) $LaMnO_3$ slabs shows that a vacancy formation energy difference is about 0.2–0.6 eV per oxygen vacancy in the explored U_{eff} range. In addition, reaction energy convergence vs number of layers in the slab is affected adversely by using the symmetric slab approach because of the change of the stoichiometry with number of layers (nonstoichiometry decays with increasing the number of layers in the symmetric slab). We therefore choose asymmetric (001) slabs with surface terminations of LaO and BO_2 to perform surface calculations in this work. We use the dipole-correction[46,47] option incorporated in the VASP code to correct for any errors associated with the surface dipole moment in the periodic calculations.

It is important that calculated energies are converged with respect to the number of layers in the slab. Convergence tests for $LaMnO_3$ surface and surface oxygen vacancy formation energies with respect to the number of layers in asymmetric slabs were performed, and the results are shown in Fig. 4. Here, only two sets of data (U_{eff}=0 eV and U_{eff}=6 eV) are shown to illustrate the influence of U_{eff} on the convergence, and it is seen that to achieve the same convergence, more layers are needed at higher U_{eff} values. Note that the surface energies shown in Fig. 4(a) are averaged surface energies of the LaO and MnO_2 terminations due to the fact that asymmetric slabs are used in our calculations. For the surface oxygen vacancy formation energy calculations shown in Fig. 4(b), the vacancy is only placed on the MnO_2 side of the slab. In order to avoid the energy fluctuation coming from the relaxation of the LaO termination, we fix the first two layers of the LaO termination to the bulk coordinates and allow atomic relaxation for the rest of layers (the same approach is also applied to surface adsorption reaction calculations). As a compromise between the convergence of surface reaction energetics and the amount of computation time, we adopt eight-layer slabs to perform surface reaction energy calculations for all the four systems [we assume that the reaction energy convergence of the other three systems will be close to that of the $LaMnO_3$ ($\lesssim$0.2 eV)]. Schematic illustrations of the (001) surface slab and surface oxygen adsorption and vacancy sites in our reaction energetic calculations are shown in Fig. 5. Note that due to symmetry breaking at the surface, distinct surface sites exist for oxygen adsorption (O-*B*, O_2-*B*, and O-bridge, which will be discussed later in

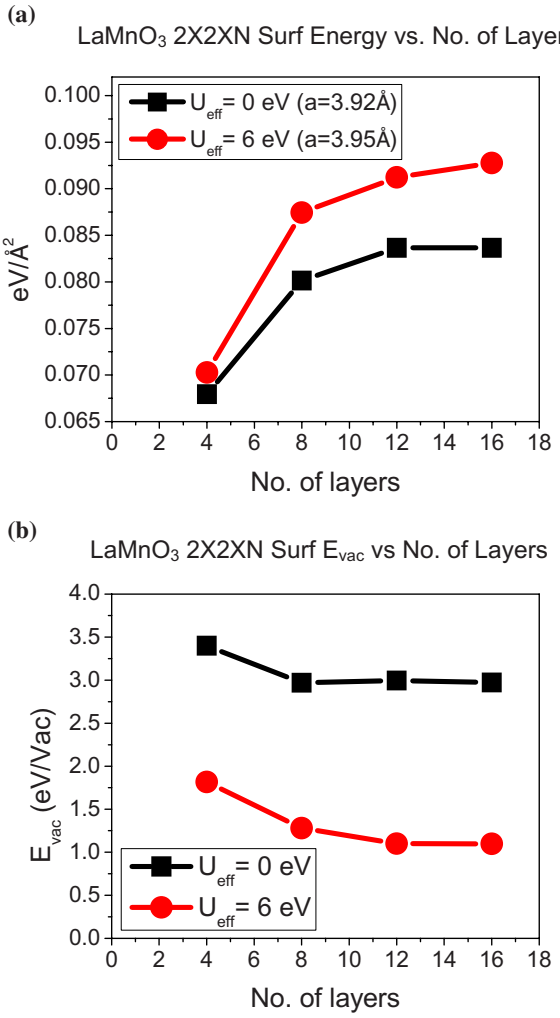

FIG. 4. (Color online) Convergence tests for (a) $LaMnO_3$ surface and (b) surface oxygen vacancy formation energies with respect to the number of layers in asymmetric slabs. In terms of the tradeoff between the energetic convergences and the amount of computation time, we adopt eight-layer asymmetric slabs to perform surface reaction energetic calculations.

Secs. II D and III B 2) and oxygen vacancies, which can cause differences in reaction energies (typically 10^{-2}–10^{-1} eV from our thorough investigations on surface reaction energies of distinct surface sites). We have generally observed that the most outward surface oxygen sites are the most stable sites for surface oxygen vacancy formation and O-bridge adsorption, and the O-*B* and O_2-*B* adsorption energies are found to be very close ($<$10 meV/O variation in the adsorption energies) for all the surface *B* sites since the surface *B* sites are identical in symmetry. For clarity, we only show results corresponding to the energetics from the most stable sites in the following discussions.

D. Reaction free energies under SOFC conditions

In order to correctly model reaction free energies under SOFC conditions (high temperature and changing PO_2) it is necessary to include a number of thermodynamic terms in addition to the zero-temperature *ab initio* energetics. The ap-

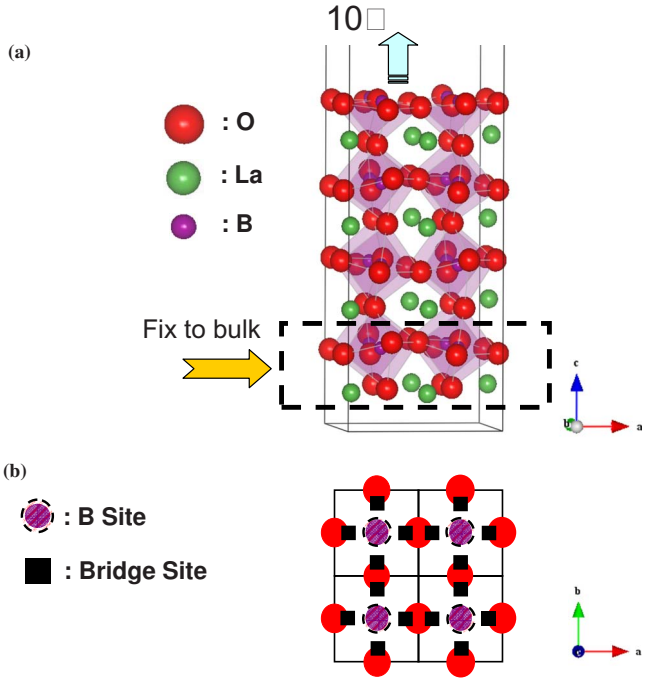

FIG. 5. (Color online) (a) A schematic illustration of the (001) eight-layer slab for LaBO$_3$ surface reaction simulations. In order to avoid the energy fluctuations coming from the relaxation of the other terminations, we fix the first two layers of the bottom termination (not involved in the surface reactions) to the bulk coordinates and allow atomic relaxation for the rest of layers. Surface reactions (oxygen vacancies and oxygen adsorption) are simulated only on the unfixed termination. (b) Top view of (001) BO$_2$ surface and locations of oxygen adsorption sites: B site and bridge site.

proach builds on the methods developed previously by a number of authors[21,48–51] and we have added an explicit term for solid phase vibrations and clarified how to include the oxygen correction discussed Sec. II B.

We first introduce the free energies for the O$_2$ gas and perfect and defected (with oxygen vacancies or oxygen adsorbates) solids. The free energies of the solids can be defined as

$$G_{solid} = E_{solid} + G_{vib} - TS_{solid} + PV_{solid}, \quad (1)$$

where E_{solid} is a lattice energy of the solid from the VASP calculation, G_{vib} is a vibrational free energy, T is temperature, S_{solids} is the configurational entropy, P is external pressure, and V_{solid} is volume. As an approximation, we neglect the energy from the PV_{solids} term since it has a relatively small energetic contribution. The G_{vib} term is assumed to be mostly canceled in LaBO$_3$ oxygen adsorption and vacancy formation reactions except for the reacting oxygen defects (vacancy or adsorbate). Since the reaction energetics investigated in this work all involve adding or removing oxygens on the surface or in the bulk, we rearrange the vibrational free energy term by removing the G_{vib} from the solid phase and combining it with the oxygen free energy expression (this adjustment will yield μ_O^{eff} defined below). Consequently, we can rewrite the Gibbs energy of the solids as

$$G_{solid} = E_{solid} - TS_{solid}. \quad (2)$$

The free energy of oxygen (normalized as per O) is equal to the oxygen chemical potential and can be approximately derived from

$$G_O = \mu_O(T,P,O_{pseud}^{ref}) = \frac{1}{2}\left[E_{O_2}^{\text{VASP}} + \Delta h_{O_2}^0 + [H_{O_2}(T,P^0) - H_{O_2}(T^0,P^0)] - TS_{O_2}(T,P^0) + kT\ln\left(\frac{P}{P^0}\right)\right], \quad (3)$$

where $E_{O_2}^{\text{VASP}}$ is the $T=0$ K energy per O$_2$ as found in the DFT calculations, $\Delta h_{O_2}^0$ is the correction for errors of the oxygen energy in O$_2$ molecules vs a solid (obtained from the oxide formation enthalpy fitting, as discussed in Sec. II B), H_{O_2} is the O$_2$ gas enthalpy, S_{O_2} is the O$_2$ gas entropy, P is the oxygen partial pressure ($P^0=1$ atm), T is temperature ($T^0=298.15$ K), and k is Boltzmann's constant. $[H_{O_2}(T,P^0) - H_{O_2}(T^0,P^0)] - TS_{O_2}(T,P^0)$ in Eq. (3) are the free energy per O of O$_2$ gas relative to the gas enthalpy at $P=P^0$ and $T=T^0$. These values are obtained experimentally (we use the polynomial fits from Ref. 52). The last term in Eq. (3) is the effect of pressure deviations from P^0.

It is convenient to define an effective oxygen chemical potential, μ_O^{eff}, as $\mu_O(T,P,O_{pseud}^{ref})$ minus the vibrational contribution to the oxygen chemical potential in the solid,

$$\mu_O^{\text{eff}} = \mu_O(T,P,O_{pseud}^{ref}) - \mu_O^{s,vib} = \mu_O(T,P,O_{pseud}^{ref}) - \tfrac{1}{2}[\bar{G}_{O_2}^{s,vib}(T) - \bar{H}_{O_2}^{s,vib}(T^0)], \quad (4a)$$

where

$$\bar{G}_{O_2}^{s,vib}(T) = k_B T \sum_j \ln\left[2\sinh\left(\frac{\theta_E}{2T}\right)\right], \quad (4b)$$

$$H_{O_2}^{s,vib}(T^0) = k_B T \sum_j \frac{\theta_E}{2T^0}\coth\left(\frac{\theta_E}{2T^0}\right), \quad (4c)$$

and $\bar{G}_{O_2}^{s,vib}(T)$ and $\bar{H}_{O_2}^{s,vib}(T^0)$ are the vibrational portions of the partial molar Gibbs free energy and enthalpy for O$_2$ in the solid and therefore give the contribution of the vibrational free energy of oxygen to the total free energy of the solid [the subtraction of $\bar{H}_{O_2}^{s,vib}(T^0)$ is necessary as this term is already accounted for in $\Delta h_{O_2}^0$]. The oxygen vibrational contribution to the solid phase is approximated with a simple Einstein model with the Einstein temperature $\theta_E=500$ K. The effective Einstein temperature was determined by diagonalizing the local force constant matrix[53] for O (all other atoms fixed) in LaMnO$_3$ and was used here as an approximate value. Changing this value by 50% in either direction (from 250 to 750 K) does not qualitatively impact any of our conclusions so no effort at a more quantitative model was attempted. An estimate for the vibrational contributions of surface oxygen species must also be made. We approximate the vibrational free energy of surface adsorbed oxygen monomers as being the same as that of lattice oxygen ions. However, the free energies of the six vibrational modes of adsorbed oxygen dimers are treated with a combination of five

mode solid oxygen vibration with θ_E=500 K plus one O_2 gas phase vibrational stretch mode with θ_E=2244 K.[54] This approximation accounts for the fact that the O_2 dimer is likely to retain a stiff O-O bond even when bonded to the surface. While these vibrational free energy terms for solid phase oxygen are very approximate, they assure that the degrees of freedom included in the gas phase (implicitly part of the experimental data) are at least represented in the solid phase. This matching of degrees of freedom will lead to significant cancellation and be more accurate at higher temperatures than simply ignoring the degrees of freedom in the solid altogether.

With the definition of the free energies of solids and the effective oxygen chemical potential shown above, the reaction free energies can be written as the free energy differences between the products and reactants. For example, the surface oxygen adsorption reaction free energy can be described as

$$\Delta G_{\mathrm{O_{ad}}} = G_{slab+\mathrm{O_{ad}}} - G_{slab} - \mu_{\mathrm{O}}^{\mathrm{eff}}, \tag{5}$$

where $\Delta G_{\mathrm{O_{ad}}}$ is the reaction free energy normalized as per oxygen, $G_{slab+\mathrm{O_{ad}}}$ and G_{slab} are the free energies of the oxygen adsorbed slab and the perfect slab, respectively, and $\mu_{\mathrm{O}}^{\mathrm{eff}}$ is the effective oxygen chemical potential.

It is useful to define the nonconfigurational contribution of reaction free energy, ΔG^*, which is equal to the reaction free energy minus the configurational entropy contribution, to estimate the energy difference between the specified initial (perfect) and final (oxygen-defected) solid states. Without configurational terms we can set G_{slab} approximately equal to E_{slab} and the ΔG^*'s of reactions can then be written as

$$\begin{aligned}\Delta G^*_{reaction} &= \Delta G_{reaction} - T\Delta S^{config}_{solid} \\ &= (E_{solid+defect} - E_{solid}) \pm \mu_{\mathrm{O}}^{\mathrm{eff}},\end{aligned} \tag{6}$$

where on the right-hand side of Eq. (5), the "+" sign is for the oxygen vacancy formation reaction and the "–" sign is for oxygen adsorption reactions.

The physical meaning of $\Delta G^*_{reaction}$ shown here is that it allows us to estimate the energy difference between the calculated defected and perfect solid states of an open system that exchanges oxygen with the surrounding environment based on the calculated *ab initio* reaction energetics. If reactions are at equilibrium, the solid phase configurational entropy contribution would cancel $\Delta G^*_{reaction}$ so that $\Delta G_{reaction}$=0.

In the following result discussions, we report zero-temperature *ab initio* reaction energetics (as opposed to reaction free energies, which include the finite temperature effects) to focus on the trends of *ab initio* energetics vs U_{eff}. The zero-temperature *ab initio* reaction energies can be obtained from Eq. (6) by setting

$$\mu_{\mathrm{O}}^{\mathrm{eff}} = \tfrac{1}{2}(E_{\mathrm{O_2}}^{\mathrm{VASP}} + \Delta h^0_{\mathrm{O_2}}).$$

The O_2 dimer in the O_2-B adsorption can have different orientations, and we have tested three O_2 dimer adsorption configurations: a vertical O_2-B, a horizontal O_2-B, and a tilted O_2-B reported in Ref. 15. The tilted O_2-B configuration is found to be the most stable one, which is 100–300 meV/O more stable than the other two configurations at U_{eff}=0 eV and at the optimal U_{eff}. We therefore use the tilted O_2-B adsorption configuration to represent the O_2-B adsorption. The three adsorption configurations, O-B, O-bridge, and O_2-B, are generally either stable or metastable (except for a few cases when they are truly unstable) and represent the only metastable adsorption configurations we identified on the surface. These configurations were also identified in Ref. 15 (with a $2\sqrt{2}\times 2\sqrt{2}$ surface instead of the 2×2 surface used in this work). These *ab initio* reaction energies will be used to investigate trends vs transitional metal types at U_{eff}=0 eV and the optimal U_{eff}.

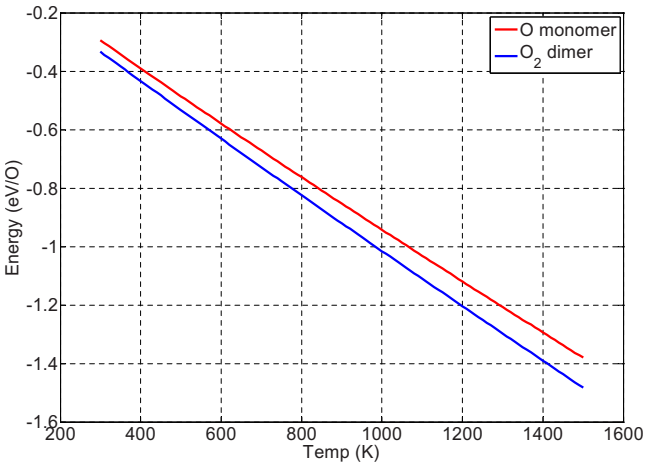

FIG. 6. (Color online) The calculated $\mu_{\mathrm{O}}^{\mathrm{eff}} - \frac{1}{2}(E_{\mathrm{O_2}}^{\mathrm{VASP}} + \Delta h^0_{\mathrm{O_2}})$ vs T at $P(\mathrm{O_2})$=0.2 atm for oxygen monomers and oxygen dimers based on Eqs. (3) and (4a).

To estimate ΔG^* vs T under SOFC conditions, we calculate $\mu_{\mathrm{O}}^{\mathrm{eff}} - \frac{1}{2}(E_{\mathrm{O_2}}^{\mathrm{VASP}} + \Delta h^0_{\mathrm{O_2}})$ vs T at $P(\mathrm{O_2})$=0.2 atm for oxygen monomers and oxygen dimers based on Eq. (3), and the results are shown in Fig. 6. The term $\mu_{\mathrm{O}}^{\mathrm{eff}} - \frac{1}{2}(E_{\mathrm{O_2}}^{\mathrm{VASP}} + \Delta h^0_{\mathrm{O_2}})$ can be added (for vacancies) or subtracted (for binding oxygen) to the zero-temperature *ab initio* reaction energies [Eq. (6)] to get the finite temperature free energies of reaction, ΔG^*, at $P(\mathrm{O_2})$=0.2 atm. The difference between the two lines in Fig. 6 comes from our different treatments of vibrational free energy contribution for the adsorbed O monomers and O_2 dimers (see above discussion in Sec. II D).

III. RESULTS

A. LaBO$_3$ bulk spin moments and electronic structures

Table II shows calculated lattice constants (a_c) of LaBO$_3$ $2\times 2\times 2$ constrained cubic (by cubic here we mean that the lattice parameters have been constrained to form a cubic cell, but the internal relaxations and symmetry are not necessarily cubic) perovskites as well as spin states, local magnetic moments (μ_B, per cation), and effective Bader charges (Q) (Refs. 55 and 56) from LaBO$_3$ bulk calculations along with experimental lattice constants[57–59] (a_c is set to be the cube root of the volume of a perovskite primitive unit cell) and reported high-temperature spin state results from the

TABLE II. Calculated lattice constants (a_c), spin states (HS: high spin; IS: intermediate spin; and LS: low spin), local magnetic moments (in μ_B per B atom), and effective Bader charges (Q) for $2\times2\times2$ LaBO$_3$ bulk perovskite. Note that the local magnetic moments are taken from the difference between projected electron density of up and down spins onto 1 Å radius sphere, while the values in parenthesis are averaged magnetic moments from the calculated total moments in the simulation cell. The corresponding optimal U_{eff} for $LaMnO_3$, $LaFeO_3$, $LaCoO_3$, and $LaNiO_3$ are 4, 4, 3.3, and 6.4 eV from Ref. 25.

		$LaMnO_3$ (AAFM)	$LaMnO_3$ (FM)	$LaFeO_3$ (GAFM)	$LaFeO_3$ (FM)	$LaCoO_3$ (FM)	$LaNiO_3$ (FM)
GGA	a_c (Å)	3.918	3.922	3.821	3.868	3.850	3.843
	Spin state	HS	HS	HS	IS/HS	IS	LS
	μ_B	3.3	3.3 (4)	3.5	2.9 (3.5)	1–2.3 (2)	0.75 (1.0)
	Q(La)	2.075	2.074	2.069	2.075	2.084	2.086
	$Q(B)$	1.699	1.703	1.498	1.577	1.476	1.294
	Q(O)	−1.258	−1.259	−1.189	−1.217	−1.186	−1.127
GGA+U, optimal U_{eff}	a_c (Å)	3.942	3.941	3.943	3.940	3.848	3.851
	Spin state	HS	HS	HS	HS	IS	LS
	μ_B	3.4–3.8	3.6 (4)	3.9	4.0 (5)	1.8–2 (2)	1.28 (1.0)
	Q(La)	2.075	2.075	2.081	2.075	2.083	2.089
	$Q(B)$	1.733	1.729	1.780	1.808	1.501	1.335
	Q(O)	−1.269	−1.268	−1.287	−1.295	−1.195	−1.141
GGA+U, U_{eff}=6 eV	a_c (Å)	3.954	3.952	3.943	3.951	3.885	
	Spin state	HS	HS	HS	HS	HS	
	μ_B	3.6–3.9	3.7–3.8 (4)	4.0	4.1 (5)	3.1 (4)	
	Q(La)	2.074	2.074	2.079	2.075	2.087	
	$Q(B)$	1.749	1.732	1.863	1.862	1.515	
	Q(O)	−1.274	−1.269	−1.305	−1.312	−1.201	
Expt. (SOFC temperature)	a_c (Å)	3.95[a]		3.93[b]		3.85–3.90[c]	3.85[b]
	Spin state	HS ($t_{2g}^3e_g^1$) [d]		HS ($t_{2g}^3e_g^2$) [e,f]		IS/HS($t_{2g}^{5-\delta}e_g^{1+\delta}$) [a]	LS ($t_{2g}^6e_g^1$) [f,g]
	μ_B	4		5		2–4	1

[a]Reference 61.
[b]Reference 58.
[c]Reference 59.
[d]Reference 32.
[e]Reference 36.
[f]Reference 60.
[g]Reference 37.

literature.[32,36,37,60,61] It is seen that the calculated lattice constants of the constrained LaBO$_3$ cubic perovskites at optimal U_{eff} show better agreement with experiments than those at U_{eff}=0 eV. Within a 1 Å radius ionic sphere, the projected local spin moments (μ_B) of B cations increase (d electrons become more localized) with increasing U_{eff}. At the optimal U_{eff}, the calculated LaBO$_3$ spin states show good agreement with experimental values. The calculated effective Bader charges in the LaBO$_3$ bulk are smaller than the formal ionic charges (La^{3+},B^{3+},O^{2-}) and change little in the explored U_{eff} range (0–6.4 eV), which suggests that the inclusion of U_{eff} only causes minor change in the LaBO$_3$ covalency (a slight reduction of the covalency as increasing U_{eff}). This also agrees with the observation of considerable covalency in $LaMnO_3$ calculated with both DFT with the pure GGA[17] and the unrestricted Hartree-Fock approach.[62]

Table III shows the calculated LaBO$_3$ band gaps at various U_{eff} and the room temperature optical band gaps reported in Refs. 63–65. The results suggest that the opening of the band gaps in the LaBO$_3$ DFT+U calculations depends on the magnetic state, J-T distortion (suppressed in the cubic structure but allowed in the orthorhombic structure), and the U_{eff} parameter. While no band gaps for all the LaBO$_3$ systems are obtained in the pure GGA calculations (at U_{eff}=0 eV) due to electron overdelocalization, the calculated band gaps at optimal U_{eff} for the orthorhombic $LaMnO_3$ and the cubic $LaFeO_3$ using the experimental antiferromagnetic ground state ($LaMnO_3$: AAFM and $LaFeO_3$: GAFM) are closer to the reported experimental band gap values. Notice that besides the magnetic structure, J-T distortion is also important for the band gap opening in $LaMnO_3$ since no band gaps are observed with the cubic structure in the explored U_{eff} range (up to 6 eV). Although the calculated gap of the ground state $LaMnO_3$ (orthorhombic AAFM phase) at the optimal U_{eff} is still underestimated (0.8 eV) as compared to the experimental values (~1 eV in Ref. 63 and ~2 eV in Refs. 64 and 65), the application of the optimal U_{eff} indeed improves both the $LaMnO_3$ band gap and the reaction energies of $\frac{1}{2}La_2O_3$

TABLE III. Calculated band gaps for LaBO_3. The corresponding optimal U_{eff} for $LaMnO_3$, $LaFeO_3$, $LaCoO_3$, and $LaNiO_3$ are 4, 4, 3.3, and 6.4 eV from Ref. 25. Due to high-temperature approximations adopted in our calculations (ferromagnetic structure with suppression of J-T distortion within in a $2\times2\times2$ cubic supercell), the calculated band gaps at the optimal U_{eff} are smaller than the experimental values (Refs. 63–65) measured at the room temperature. The smaller band gaps at the optimal U_{eff} in our calculations could correspond to the higher electronic conductivity at the SOFC operating temperature.

	$LaMnO_3$				$LaFeO_3$		$LaCoO_3$	$LaNiO_3$
	FM (cubic)	AAFM (cubic)	FM (ortho.)	AAFM (ortho.)	FM (cubic)	GAFM (cubic)	FM (cubic)	FM (cubic)
GGA, U_{eff}=0 eV	0	0	0	0	0	0	0	0
GGA+U, optimal U_{eff}	0	0	0	0.8	0.7	2.0	0.02	0.0
GGA+U, U_{eff}=6 eV	0	0	0	0.8	2	2.5	0.6	
Expt.			1.0,[a] 2.0[b]			2.1[a]	0.3[a]	0.0[a]

[a]Reference 63.
[b]References 64 and 65.

$+MnO_x+\frac{1}{2}(\frac{3}{2}-x)O_2\rightarrow LaMnO_3$ (shown in Fig. 3) as compared to those with the pure GGA. In addition, because the $LaMnO_3$ band gap disappears above $T_{J\text{-}T}$ (750 K),[64] the high-temperature cubic structure with no band gap (suppression of J-T distortion) instead of the insulating ground state orthorhombic phase is used in the following $LaMnO_3$ surface ORR energetic calculations to simulate reactions under SOFC conditions. Therefore, the error in the band gap of the low-temperature $LaMnO_3$ phase at the optimal U_{eff} is unlikely to have significantly impact on the calculated reaction energetics at high temperatures. The band gap of $LaCoO_3$ is narrow and sensitive to the spin state and magnetic structure. $LaCoO_3$ undergoes spin state transitions with increasing temperatures (low spin to intermediate spin), which causes difficulty in reproducing the $LaCoO_3$ band gap measurement from experiments (0.14 eV in Ref. 61 and 0.3 eV in Ref. 63). In this work, the band gap value for the cubic and ferromagnetic $LaCoO_3$ at optimal U_{eff} is 0.02 eV, which is lower than the experimentally reported values and could be attributed to the adoption of the cubic structure (suppression of the J-T distortion) and the ferromagnetic state for the intermediate spin $LaCoO_3$ ($t_{2g}^5e_g^1$). However, since $LaCoO_3$ exhibits higher electronic conductivity at high temperatures (T_{JT}=500 K) and there has also been reported surface ferromagnetism in $LaCoO_3$,[66] we also expect that surface ORR energetics under SOFC conditions will be better described by our approximation to the high-temperature structure than by fully relaxed low-temperature structures. Finally, both pure GGA and the optimal U_{eff} results predict no band gap for $LaNiO_3$, consistent with experimental results.

Figure 7 shows the spin-polarized total density of states (TDOS) and partial density of states (PDOS) for the perfect $2\times2\times2$ bulk of the LaBO_3 systems at U_{eff}=0 eV and the optimal U_{eff}, where the Fermi energy is aligned at zero. The DOSs are normalized to number of states per eV per simulated bulk supercell (a $2\times2\times2$ supercell which consists of 40 atoms). It is seen that the electronic structures are significantly changed by including U_{eff}, and the band shifts driven by the U_{eff} shown in Fig. 7 agree with other LDA+U studies for strongly correlated transition metal oxides.[4,8,19,67] In particularly, O $2p$ orbitals are shifted toward the Fermi surface, occupied transition metal $3d$ states are shifted to the lower valence bands, and unoccupied states are moved to the upper conduction bands. Although U_{eff} is applied only to the transition metal, the upshift of the O $2p$ states in the DOS plots can be explained by the downshift of occupied $3d$ orbitals (as well as the Fermi energy level) with respect to O $2p$ bands. Since the Fermi surface energy is aligned at 0, the O $2p$ orbitals are therefore shifted up with respect to the Fermi surface when U_{eff} is increased.

In comparing the e_g PDOS plots of the calculated LaBO_3 systems, we notice that the unoccupied $e_g\uparrow$ states of FM and AAFM $LaMnO_3$ ($t_{2g}^3e_g^1$), intermediate spin FM $LaCoO_3$ ($t_{2g}^5e_g^1$; $LaCoO_3$ becomes high spin as $U_{eff}\geq6$ eV), and FM $LaNiO_3$ ($t_{2g}^6e_g^1$) are less affected by U_{eff} than unoccupied states of $LaFeO_3$ and remain close to the Fermi energy level at the optimal U_{eff}. However, in both FM and GAFM $LaFeO_3$ ($t_{2g}^3e_g^2$) a significant band gap is opened. Similar results are also reported by Yang *et al.*,[8] who suggested that the characteristics of $LaFeO_3$ band gap with respect to U (U and J are different parameters in Ref. 8) are different from $LaMnO_3$ and $LaCoO_3$. Yang *et al.* reported that the gap of $LaFeO_3$ is always increased (from 0.5 to 3.2 eV between U=0 and U=11 eV) with the increase of U, while the gap of $LaMnO_3$ or $LaCoO_3$ is small ($\leq$0.8 eV between U=0 and U=11 eV) and less affected by U, which may be due to the more itinerant property of $e_g\uparrow$ states.[7] The distinct band gap vs U trend (or U_{eff} in this work) in $LaFeO_3$ results in an increase of reaction energetics associated with electron doping (e.g., oxygen vacancy formation energy) as one increases U_{eff}, while for $LaMnO_3$, $LaNiO_3$, and intermediate spin $LaCoO_3$ ($U_{eff}<6$ eV) with small or no band gaps, the reaction energies associated with electron doping are decreased as increasing U_{eff}. These trends will be discussed further in Sec. III B 1.

While the U and J (or U_{eff}) for LaBO_3 in the literature can vary depending on how the parameter(s) are obtained (e.g., self-consistent U,[68] fitting band gap, electronic structure, or energetics), we believe that the electron overdelocalization in LDA/GGA could introduce significant errors in ORR energetics for the LaBO_3 systems. The optimal U_{eff} adopted in this work are fit with redox energetics of BO_x transition metal oxides, which is consistent with the focus in this work (reaction energetics associated with reduction or oxidation

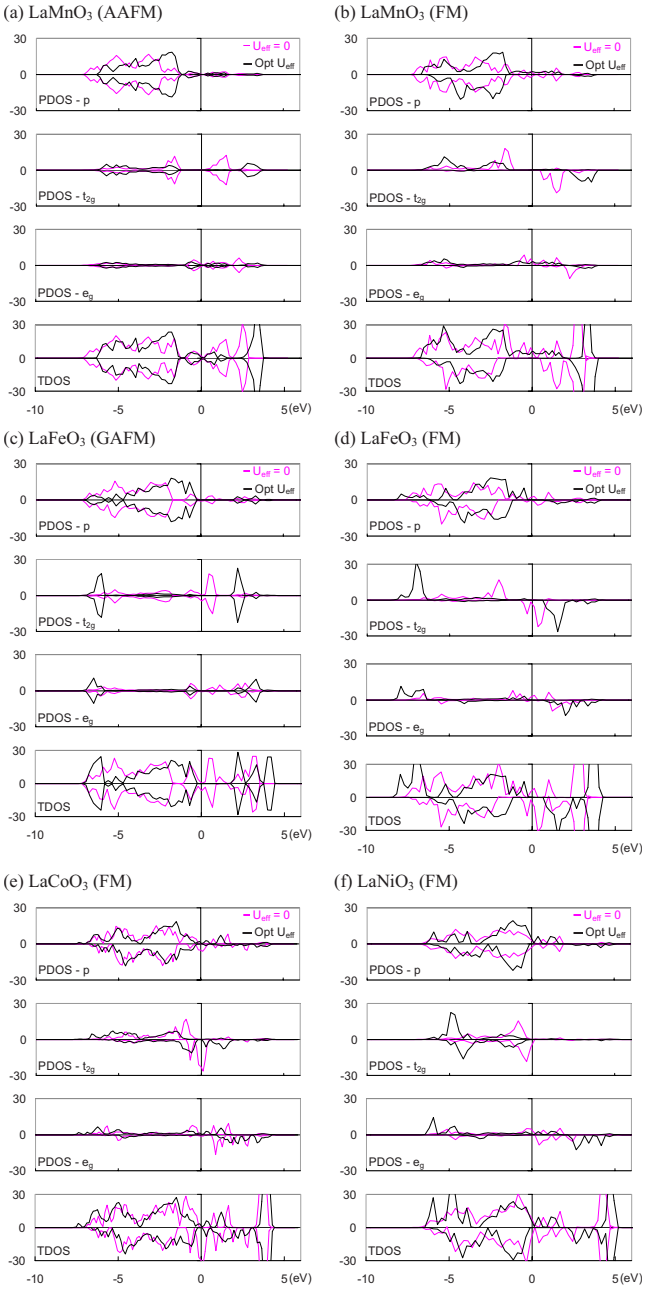

FIG. 7. (Color online) (a) $LaMnO_3$ (AAFM), (b) $LaMnO_3$ (FM), (c) $LaFeO_3$ (GAFM), (d) $LaFeO_3$ (FM), (e) $LaCoO_3$ (FM), and (f) $LaNiO_3$ (FM) bulk DOS plots. From top to bottom: projected p PDOS, projected t_{2g} PDOS, projected e_g PDOS, and TDOS. DOS is in units of states per eV per $2\times2\times2$ unit cell.

on B cations). It is also demonstrated in Fig. 3 that the use of the optimal U_{eff} can improve $LaBO_3$ formation energy accuracy as compared to those with the pure GGA. In addition, the calculated lattice constants, magnetic moments, and band gaps at optimal U_{eff} are in better agreement with experimental values than those with the pure GGA. Finally, assuming the use of the optimal U_{eff} in this work for $LaBO_3$ systems still suffers from some degree of uncertainty (e.g., errors in experimentally measured energetics, different U_{eff} for surface and bulk, etc.), the energetics vs U_{eff} results shown in Sec. III B suggest that variations of U_{eff} by ±1 eV would only change reaction energetics by a few hundred meV, which would not qualitatively change the ORR trend discussions in this work.

B. Energetics vs U in $LaBO_3$

1. Oxygen vacancy formation energies vs U_{eff}

The O vacancies are important for the ORR in SOFCs as they are likely to couple strongly to oxygen dissociation, transport, and incorporation. For the two types of (001) surface terminations (LaO and BO_2), it is found that the LaO surface consistently exhibits higher (more positive) O vacancy formation energy and stronger (more negative) O adsorption energies than BO_2 surfaces (values between the surfaces typically differ by 1–3 eV). Note that LaO surfaces are modeled analogously to the BO_2 surfaces by freezing the two layers farthest from the surface at bulk positions. An explanation for the higher O affinity of the LaO compared to the BO_2 termination can be found in a simple bond breaking picture. In creating the two types of surfaces from cleavage of bulk, the BO_2 termination has only one broken B-O bond, while the LaO termination has four broken La-O bonds. Since the relaxed surfaces do not undergo severe surface reconstructions, this simple ionic bond breaking picture should be a qualitative guide for understanding the two surfaces. We expect that the LaO oxygen affinity will be greater than that of BO_2 due to the already reduced bonding creating a higher driving force to recover the La-O bonds or similarly resist further La-O bond breaking. The generally higher O vacancy formation and stronger O adsorption energies suggest that LaO termination could be catalytically inactive for ORR in SOFCs. The higher O vacancy formation energies imply that there will be fewer vacancies on the surface, which will likely reduce active sites for O_2 splitting and/or O incorporation into the bulk. Surface O transport will likely be slower due to having few vacancies near the surface and possibly increased kinetic barriers (which are often correlated with oxygen binding strength[69]). In addition, the strong oxygen binding may lead to a high coverage of dissociated oxygen, effectively passivating the surface. Therefore, in the following surface energetics vs U_{eff} discussion, we focus on reaction energetics of the BO_2 surface.

Figure 8 shows the U_{eff} dependence of bulk and surface oxygen vacancy formation energies (E_{vac}) for $LaBO_3$ (B =Mn, Fe, Co, and Ni) systems. The calculations were performed using $2\times2\times2$ cubic supercells and eight-layer slabs with 2×2 (001) surfaces for bulk and surfaces, respectively. Within the explored U_{eff} range, E_{vac}'s at (001) BO_2 surfaces are found to be about 1–2 eV more stable than in the bulk, which suggests that vacancy concentrations at (001) BO_2 surfaces will be dramatically higher than in the bulk. Both bulk and BO_2 surface E_{vac} are decreased by 1–2 eV from U_{eff}=0 to U_{eff}=6 eV except the $LaFeO_3$ bulk (both FM and GAFM), which is increased by about 0.5 eV from U_{eff}=0 to U_{eff}=6 eV. Piskunov *et al.*[21] reported that oxygen vacancy formation energies in $La_{7/8}Sr_{1/8}MnO_3$ bulk and on the MnO_2 terminated surface calculated with the hybrid B3LYP exchange-correlation functional, which also corrects the self-interaction errors by introducing a certain degree of Fock

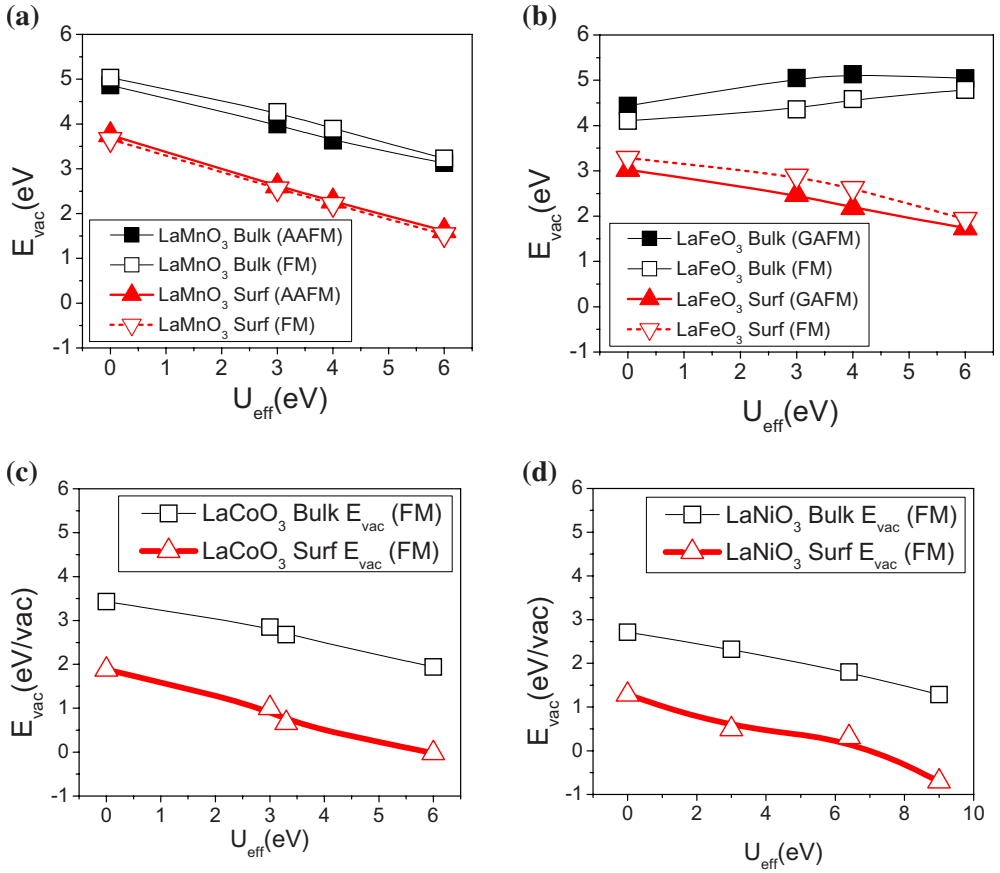

FIG. 8. (Color online) (a) $LaMnO_3$, (b) $LaFeO_3$, (c) $LaCoO_3$, (d) $LaNiO_3$ bulk, and (001) BO_2 surface oxygen vacancy formation energies (E_{vac}) vs U_{eff}. All the E_{vac} values shown in the figures have been corrected with the O_2 correction.

exchange, are 2.7 and 2.2 eV, respectively. The calculated MnO_2 surface oxygen vacancy formation energy shows excellent agreement with our calculated value (also 2.2 eV) at optimal U_{eff}. On the other hand, the $La_{7/8}Sr_{1/8}MnO_3$ bulk oxygen vacancy formation energy is 1.2 eV lower than our $LaMnO_3$ bulk E_{vac} at the optimal U_{eff}, which could easily be due to oxidation of Mn^{3+} by Sr doping and Sr-oxygen vacancy interaction. The unexpected trend in $LaFeO_3$ is explained in terms of the electronic structure below. The E_{vac} vs U_{eff} trends shown here mostly agree with other DFT+U studies on the redox energetics of late transition metal or rare-earth metal oxides,[25,38,70] where a general observation is that adding U_{eff} stabilizes the reduction products and decreases the reduction energy and vice versa for oxidation energy (destabilizes the oxidation products and increases the oxidation energy). This effect is generally attributed to the reduction of the self-interaction of the reduced products by the U_{eff} value.

In Fig. 9, we report the LaBO_3 perfect and defected (containing a vacancy) bulk TDOSs and surface PDOSs at U_{eff} =0 eV and optimal U_{eff}, where the surface PDOSs are taken from the top two relaxed surface layers of the slabs and are normalized to give the same integral as the TDOSs (which are normalized to give number of states per eV per $2\times2\times2$ supercell). The oxygen vacancy formation reaction is associated with electron doping, which in a metallic rigid band model will slightly shift the DOS down in energy relative to the Fermi surface. Consistent with this model, it is generally seen that the oxygen vacancy bulk TDOSs and surface PDOSs are similar to those of the corresponding undefected systems but slightly shifted downward both in pure GGA and GGA+U. There are three exceptions to this shift in Fig. 9: the 1.2, 0.7, and 0.8 eV downshifts of the whole electronic structure for the defected $LaFeO_3$ GAFM bulk, FM bulk, and GAFM surface at the optimal U_{eff}, respectively. These abnormally large electronic structural shifts in both the oxygen-defected $LaFeO_3$ FM and GAFM bulk at the optimal U_{eff} can be attributed to the systems half filled d-shell characteristics and large band gaps. When electrons liberated from the oxygen by creating a vacancy are doped into the high spin $LaFeO_3$ bulk, the new electrons have to overcome the band gap and be placed into the unoccupied $t_{2g}\downarrow$ orbitals (conduction band), which at U_{eff}=4 eV are found to be ~0.7 eV above the Fermi surface for $LaFeO_3$ FM bulk or into new defected states in the gap, as shown in the PDOS plots of the defected $LaFeO_3$ GAFM bulk at optimal U_{eff}. As for the $LaFeO_3$ GAFM surface at the optimal U_{eff}, it is predicted to be metallic (this will be explained below), but the creation of surface oxygen vacancies in our surface model introduces more electrons than can be held by the unoccupied states near the Fermi surface. Therefore, extra electrons continue to fill in new defect states in the gap as the unoccupied states near the Fermi energy level are no longer available and cause a 0.8 eV shift of the whole elec-

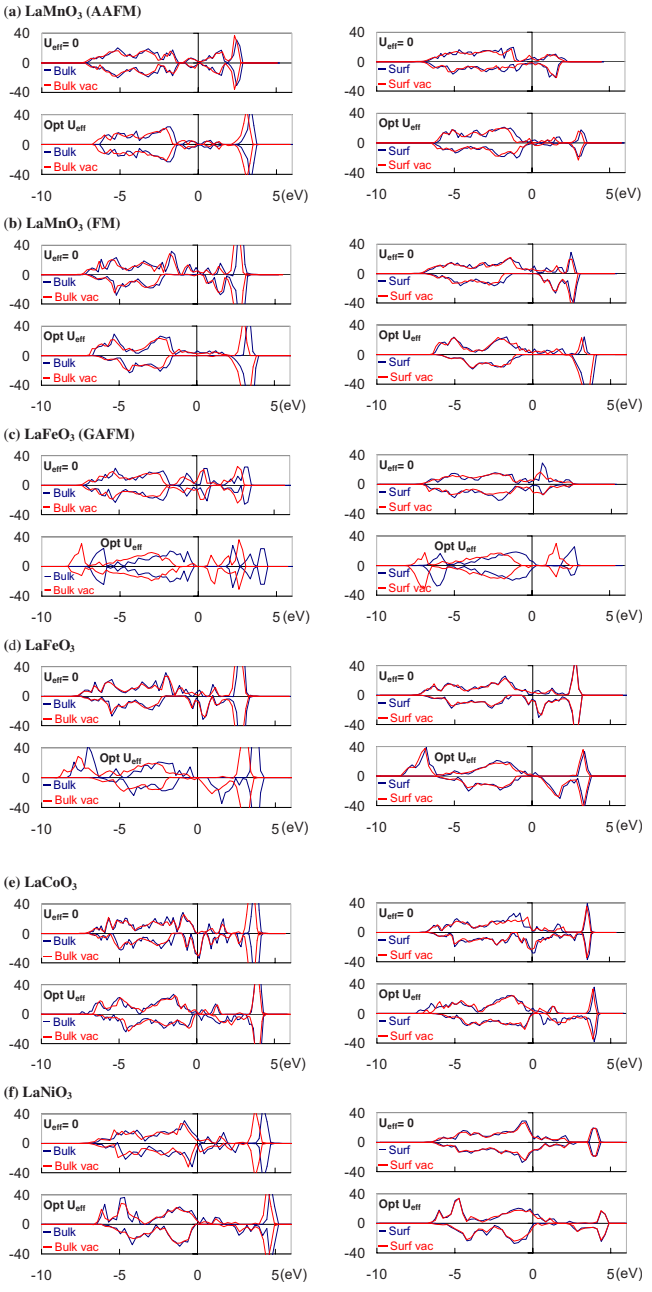

FIG. 9. (Color online) (a) $LaMnO_3$ (AAFM), (b) $LaMnO_3$ (FM), (c) $LaFeO_3$ (GAFM), (d) $LaFeO_3$ (FM), (e) $LaCoO_3$ (FM), and (f) $LaNiO_3$ (FM) perfect vs with a vacancy bulk TDOS and surface PDOS at U_{eff}=0 eV and at optimal U_{eff}. The surface PDOSs are taken from the top two relaxed surface layers of the slabs and are normalized to give the same integral as the TDOSs.

tronic structure. On the other hand, at U_{eff}=0 eV, Fe^{3+} *s* in the $LaFeO_3$ bulk and surface (both FM and GAFM) are not in the high spin state and electrons are more delocalized, so that $LaFeO_3$ is predicted to be metallic at U_{eff}=0 eV and a far smaller shift of electronic structure is observed from the vacancy. Within the explored U_{eff} range, for $LaMnO_3$, intermediate spin $LaCoO_3$ ($U_{\text{eff}}<6$ eV), and $LaNiO_3$ bulk and surfaces, the doping electrons from the oxygen vacancy are able to fill the unoccupied $e_g\uparrow$ states. These states are relatively insensitive to U_{eff} and are located near the Fermi surface with very small or no gap. Consequently, the electronic structures are only slightly shifted down when doping electrons in $LaMnO_3$, intermediate spin $LaCoO_3$, and $LaNiO_3$.

The behavior of $LaFeO_3$ is particularly interesting, as the bulk and surface are predicted to have dramatically different electronic structures. While the bulk is insulating, with a significant gap, the FeO_2 surface has a more metalliclike band structure. This is due to off stoichiometry of the surface layers, where the Fe cations near the FeO_2 termination are likely to be more oxidized and those near the LaO surface will be more reduced. Therefore, both the $LaFeO_3$ FM and GAFM FeO_2 surface PDOS plots in Figs. 9(c) and 9(d) show extra unoccupied states with no gap near the Fermi surface as compared to their bulk at U_{eff}=4 eV. While the doping of electrons in $LaFeO_3$ bulk significantly shifts up the Fermi energy level (downshifts the whole electronic structure) due to its larger band gap, the $LaFeO_3$ FM surface does not exhibit an analogous shift [Fig. 9(c)]. This is because electrons can still fill in the unoccupied majority *d* states as oxygen vacancies are introduced to the $LaFeO_3$ (001) FeO_2 surface. The reason for the 0.8 eV global shift of the electronic structure for the defected $LaFeO_3$ GAFM FeO_2 surface has been explained above. However, we note that if a smaller surface oxygen vacancy concentration was used then the unoccupied states near the Fermi surface could contain the additional electrons, the added electrons would just fill these unoccupied states near the Fermi surface level, and the 0.8 eV downshift of whole electronic structure would not occur. The large band gaps in the bulk electronic structures, which increase with U_{eff}, make it increasingly difficult to reduce the systems as U_{eff} increases. This trend gives rise to the anomalous upward slope of the vacancy formation energy in Fig. 8(b), as the doping electrons are forced into new defected states in the band gap or even higher energy unoccupied $t_{2g}\downarrow$ orbitals. On the other hand, as oxygen vacancies are introduced to the $LaFeO_3$ FM (001) FeO_2 surface, electrons can still fill in the unoccupied states near the Fermi surface due to the already partially oxidized FeO_2 termination. Therefore, the electron doping in the $LaFeO_3$ FM (001) FeO_2 surface from surface oxygen vacancies only produces a small shift of the Fermi surface as the electrons just fill these unoccupied states near the Fermi surface. Since increasing U_{eff} lowers the Fermi energy level, the surface vacancy formation energy in $LaFeO_3$ FM (001) FeO_2 decreases with U_{eff}. The oxygen vacancy formation energy of $LaFeO_3$ GAFM (001) FeO_2 surface also decreases with increasing U_{eff}, but the electronic structure of the defected surface exhibits a significant 0.8 eV global shift at the optimal U_{eff}, which is similar to those shifts seen in the defected bulk (at optimal U_{eff}). However, these $LaFeO_3$ GAFM surface oxygen vacancy energies shown here are likely to correspond to a mixed energy of filling two different bands, i.e., the unoccupied states near the Fermi surface of the partially oxidized FeO_2 undefected surface, and the new defect states in the gap from the spillover of the doping electrons. The first should have a similar U_{eff} dependence of the vacancy formation energy seen in the $LaFeO_3$ FM surface. The later is responsible for such significant electronic structure shift as these new defect band states become the highest occupied states. If these defect states have more conduction band character then their energy will

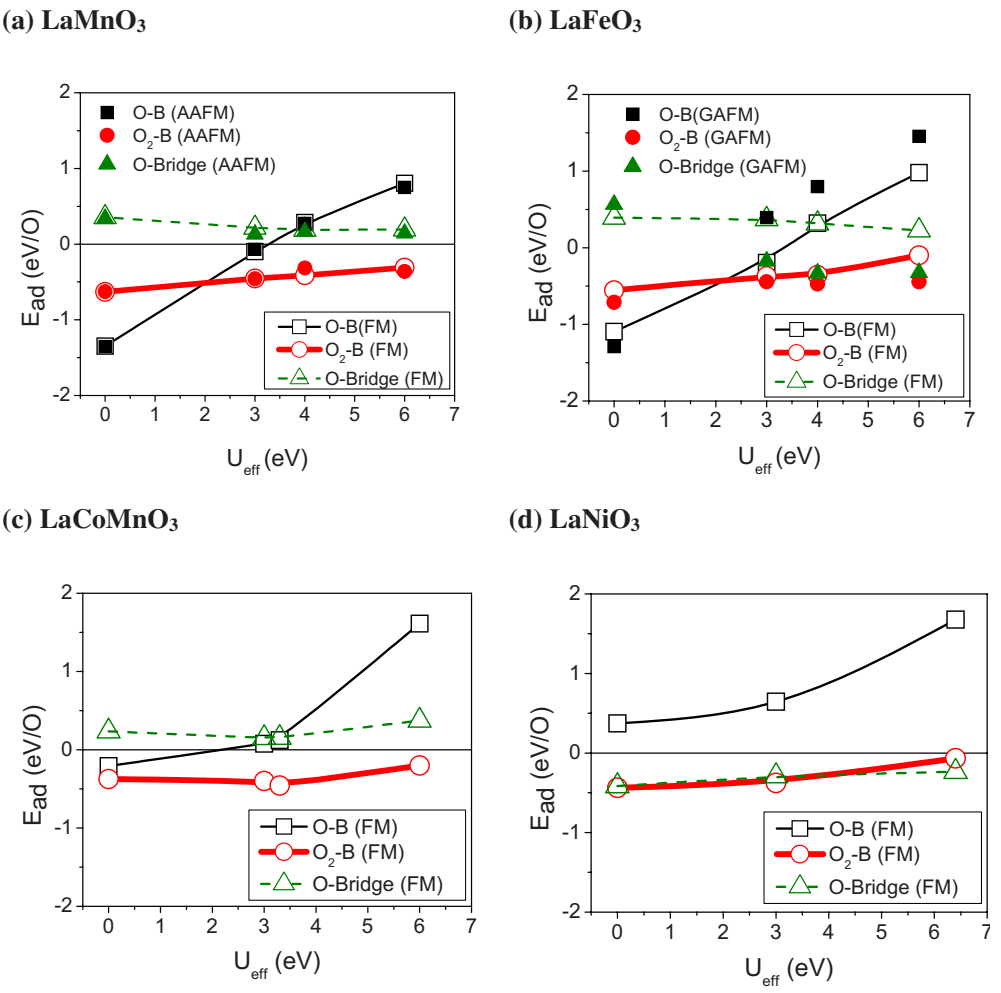

FIG. 10. (Color online) Three types of (001) BO_2 surface oxygen adsorption energies (per O) vs U_{eff}: O-*B*, O-bridge, and O_2-*B* for (a) $LaMnO_3$, (b) $LaFeO_3$, (c) $LaCoO_3$, and (d) $LaNiO_3$. All the E_{ad} values shown in the figures are corrected with the O_2 correction (0.33 eV/O_2).

shift with the conduction band and it will cost more energy to fill these states as increasing U_{eff} due to the increase of the band gap (which is similar to bulk vacancy formation energy vs U_{eff}). On the other hand, if these defect band states exhibit more valence band character then they will shift with the valence band and follow the downshift of the Fermi energy level with increasing U_{eff}. Because the overall trend shows $LaFeO_3$ GAFM FeO_2 surface oxygen E_{vac} decreases as increasing U_{eff}, it is either the case that the contribution from the defect band states is relatively small compared to the unoccupied states near the Fermi surface or the case that the defect band states exhibit valence band characteristics. Overall, the $LaFeO_3$ surface E_{vac} vs U_{eff} trends with FM and GAFM structures are similar (E_{vac}'s are decreased as increasing U_{eff}) and opposite to their bulk E_{vac} vs U_{eff} (E_{vac}'s are increased as increasing U_{eff}). However, there is an ~0.5 eV approximately constant shift between the E_{vac} values in the FM and GAFM states, which is also seen in the bulk E_{vac}'s (but in the opposite direction). Such constant shifts originate from the essential electronic structure difference between the $LaFeO_3$ FM and GAFM states. Further discussion on E_{vac} and other ORR relevant energetics vs electronic structures will be summarized in a future paper. In this paper, we focus only on understanding the trends in ORR energetics vs U_{eff} and quantifying the magnetic energy contributions if they are significant.

2. Oxygen adsorption energies vs U_{eff}

Figure 10 shows the three types of the LaBO_3 (001) BO_2 surface oxygen adsorption energies (per O) vs U_{eff}: (1) O-*B*, (2) O-bridge, and (3) O_2-*B*, where the adsorption energies are referenced to an isolated O_2 molecule far away from the surface. The three O adsorption configurations correspond to three distinct charge states for surface oxygen:[15,16] (1) is the dissociated O^{2-} state, (2) is the peroxide (O_2^{2-}) state, and (3) is the superoxide (O_2^{-}) state. In Ref. 15, it is reported that with PAW potentials and GGA-PW91, the order of the adsorption energies for these three types of adsorption on the $LaMnO_3$ (001) MnO_2 surface is (1)−1.07 eV/O>(2) −0.57 eV/O>(3)0.54 eV/O, where the three adsorption energies are very close to our $LaMnO_3$ values at U_{eff} =0 eV, with less than <0.2 eV difference (note that the sign convention of adsorption energy between Ref. 15 and this work is opposite—all values here are given with the sign convention of this work, and the surface area is two times larger than the one used in this work). In terms of the *ab*

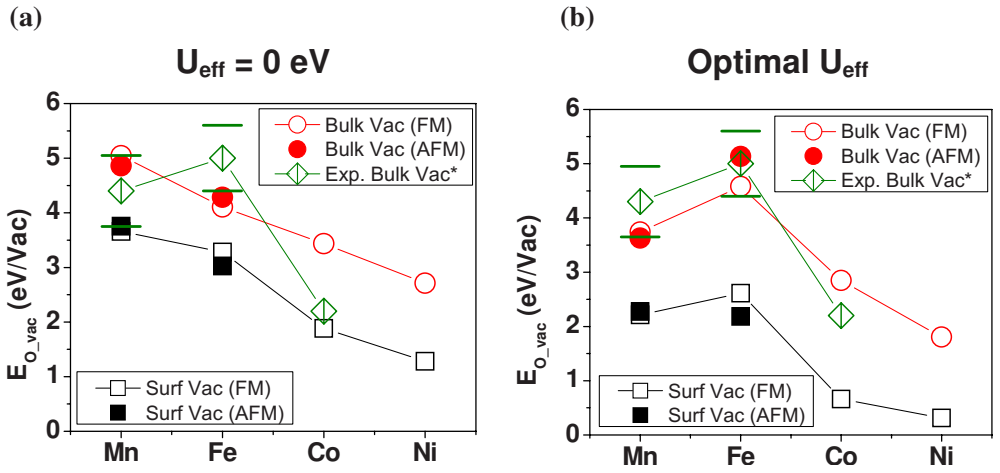

FIG. 11. (Color online) LaBO_3 bulk and BO_2 surface vacancy formation energies vs transition metal types (B=Mn, Fe, Co, and Ni) (a) at U_{eff}=0 eV and (b) at optimal U_{eff}'s. The experimental oxygen vacancy formation enthalpy data (with error bars) are taken from Refs. 71 and 72 for $LaMnO_3$, Ref. 73 for $LaFeO_3$, and Ref. 74 for $LaCoO_3$. The fitted oxygen vacancy formation reaction is $2B^x+O^x \leftrightarrow 2B'+V_O^{\bullet\bullet}+\frac{1}{2}O_2$ (Kröger-Vink notation).

initio adsorption energy results in Ref. 15, Kotomin *et al.* suggested that the dissociative oxygen adsorption is favorable on the $LaMnO_3$(001) surface due to $2E_{\text{ad}}(O) > E_{\text{ad}}(O_2)$. However, when calculations are performed under the GGA $+U$ scheme, the three adsorption energies exhibit dissimilar U_{eff} dependences, and the order of the energetic stability for the three adsorptions is different at different U_{eff} values, as shown in Fig. 9. These dependences are consistent with the general trends of the oxidation energies[25,38,70] with U_{eff}, from which we expect that the more oxidation of the surface B ions involved in the surface species, the stronger the U_{eff} dependence (a more positive slope in Fig. 10). Among the three O adsorption states, the O-B adsorption has the strongest oxidation of B's (forming an O^{2-} adatom takes two electrons out of the system). Weaker U_{eff} dependence is observed for the O_2-B adsorption (forming an O_2^- takes 1 electron out of the system). The O-bridge adsorption has no clear trend in its U_{eff} dependence because the formation of the O_2^{2-} peroxide by an O-bridge adatom bound with a lattice O^{2-} does not remove electrons from of the system. The differences associated with magnetic structure for the $LaMnO_3$ oxygen adsorption energies are not significant (within $\pm$0.2 eV between FM and AAFM states). However, the changes in oxygen adsorption energies between the FM and GAFM states for $LaFeO_3$ are very large. For significant U_{eff}, the magnetic energy contribution causes a 0.6–0.7 eV/O shift in O-B and O-bridge E_{ad}'s and a 0.2–0.3 eV shift in O_2-B E_{ad}, which suggest that magnetic structure has significant influence on the $LaFeO_3$ oxygen adsorption energies. Relatively smaller differences (within $\pm$0.2 eV) of E_{ad}'s with respect to different magnetic states are found in the pure GGA calculations, which are due to the incorrect prediction of metallic $LaFeO_3$ for both the GAFM and FM states. Overall, the O_2-B adsorption remains as the most stable configuration between U_{eff}=3 and 6 eV (in both FM and GAFM states), but the binding strengths of E_{ad}(O-bridge) and E_{ad}(O-B) will depend on magnetic states and the U_{eff} value. We have also observed that changes in spin states are coupled with the adsorption energies for the $LaCoO_3$ and $LaNiO_3$ systems, and spin value is quite sensitive to U_{eff}. Therefore, for the $LaCoO_3$ and $LaNiO_3$ both spin and adsorption energies exhibit some significant degree of nonlinearity with U_{eff}. However, as seen in Fig. 10, the scale of the adsorption energy U_{eff} dependence for the two systems is greater than that of the spin fluctuation energy vs U_{eff}, so the adsorption energy vs U_{eff} trends are qualitatively similar to that expected from simple oxidation energy arguments. Also, due to the more metallic characteristics of $LaCoO_3$ and $LaNiO_3$, the magnetic energy contributions to all the three E_{ad}'s for the two systems are expected to be much smaller than those seen in $LaFeO_3$ and within the targeted accuracy range of this work ($\pm$0.2 eV).

C. LaBO_3 reaction energetics vs transition metal types

1. Oxygen vacancy formation energy vs B

The calculated LaBO_3 bulk and surface E_{vac} at U_{eff} =0 eV and optimal U_{eff} as well as the experimental bulk vacancy formation enthalpies obtained from thermogravimetry experiments for $LaMnO_3$,[71,72] $LaFeO_3$,[73] and $LaCoO_3$ (Ref. 74) are shown in Fig. 11. It is noted that the experimental oxygen vacancy formation reaction enthalpies are taken from the following reaction (expressed in terms of the Kröger-Vink notation), $2B^x+O^x \leftrightarrow 2B'+V_O^{\bullet\bullet}+\frac{1}{2}O_2$, in order to match with the energetics obtained from our DFT simulations. The calculated bulk and BO_2 surface E_{vac} are ordered as Mn > Fe > Co > Ni at U_{eff}=0 eV and Fe > Mn > Co > Ni at the optimal U_{eff}. Since including U_{eff} generally decreases E_{vac}, both bulk (except for $LaFeO_3$) and surface E_{vac}'s of each system at the optimal U_{eff} are lower than those at U_{eff} =0 eV. We find that using the optimal U_{eff} gives bulk vacancy formation energies in the correct order (Fe > Mn > Co), as opposed to U_{eff}=0 eV (Mn > Fe > Co), and the E_{vac}'s at optimal U_{eff} are closer to the experimental values than at U_{eff}=0 eV. We also find that the order of the LaBO_3 optimal U_{eff} E_{vac} agrees with the order of LaBO_3 thermoreduction temperatures ($LaFeO_3$: 1833 K > $LaMnO_3$: 1353 K

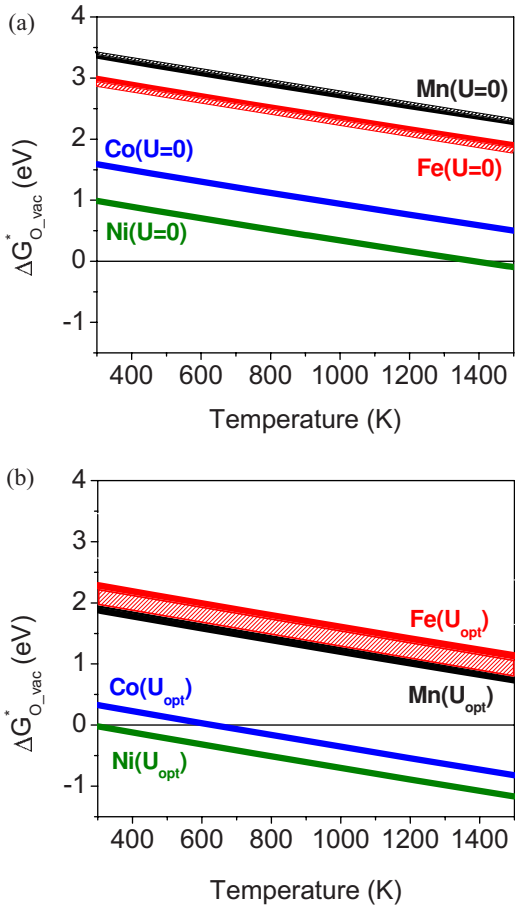

FIG. 12. (Color online) Surface ΔG^*_{vac} for $LaMnO_3$ (black), $LaFeO_3$ (red), $LaCoO_3$ (blue), and $LaNiO_3$ (green) at (a) U_{eff} =0 eV and (b) at optimal U_{eff} as a function of temperature at $P(O_2)$=0.2 atm. Shaded areas specify the possible BO_2 surface oxygen vacancy formation energy range between the ferromagnetic state (given by the line) and the ground state antiferromagnetic state as the other boundary.

$>LaCoO_3$:1173 K$>LaNiO_3$:873 K) reported in Refs. 75 and 76. Although the optimal U_{eff} still give discrepancies compared to experiment in E_{vac} of up to 0.5 eV, this is consistent with the $\sim\pm0.6$ eV (Refs. 72 and 73) error bars on the $LaMnO_3$ and $LaFeO_3$ experimental values and the true errors may be significantly less than 0.5 eV. The larger energy deviation from experimental oxygen vacancy formation enthalpies and incorrect order of E_{vac} at U_{eff}=0 eV do suggest that large errors ($\sim$1 eV) exist for vacancy energies with pure GGA/LDA for LaBO_3 systems. The dramatic improvement in order and overall error suggests that using optimal U_{eff} leads to more accurate defect reaction energetics.

To further understand oxygen vacancy formation reactions under SOFC conditions, we use Eq. (6) to estimate reaction free energies of LaBO_3 surface ΔG^*_{vac} vs temperature at $P(O_2)$=0.2 atm, both for U_{eff}=0 eV and for the optimal U_{eff}. The results are shown in Figs. 12(a) and 12(b), respectively. Since the oxygen chemical potential is greatly stabilized by the large entropy contribution in the O_2 gas phase, all the ΔG^*_{vac} decreased as temperature increases. At the optimal U_{eff} [Fig. 12(b)], the reaction free energies for Ni and Co are negative over a significant temperature range, which might seem to suggest that the surfaces are unstable under these PO_2 and temperature conditions. However, these are surface defect reaction energies for isolated O vacancies in an otherwise undefected LaBO_3 structure. This ignores potentially quite large effects associated with the presence of other defects (e.g., cation vacancies in $LaMnO_3$), defect interactions (e.g., oxygen vacancy-vacancy repulsion or ordering), and changes in the overall Fermi level due to off stoichiometry. For example, for $La_{1-x}Sr_xCoO_{3-\delta}$, an almost linear decrease in the oxygen chemical potential is found with increasing net electron concentration.[77] Such behavior is explained by the increase of Fermi energy level upon the filling of the electronic bands with the electrons introduced by oxygen vacancy formation and/or Sr doping (a rigid band model). Since our LaBO_3 perfect vs oxygen-defected DOS plots shown in Fig. 9 approximately follow a rigid band model, our calculated oxygen vacancy formation energies are expected to be dependent on the change of the Fermi energy level from electron or hole doping. Therefore, as more oxygen vacancies are formed the Fermi energy level is increased, and the reaction energy of introducing the next oxygen vacancy will also be increased. These more complex defect interactions can help stabilize the surface at higher vacancy concentrations.

It is interesting to see to what extent we can validate the calculated surface and bulk vacancy energetics with respect to results of temperature programmed desorption (TPD) experiments.[75,78–80] TPD experiments show peaks representing desorption of surface lattice oxygen (β oxygen) at about >1100 K (Fe), 1000–1100 K (Co), 800–1100 K (Mn), and 500–1100 K (Ni). Thermodynamically, we expect that a large peak in TPD associated with surface lattice oxygen will correlate with the vacancy formation reaction free energy reaching a value near or below zero, although kinetic factors are involved in the TPD experiments, which are not calculated in this work. We can therefore at least qualitatively compare the trends of the temperatures where the predicted vacancy formation free energies cross zero (see Fig. 12) with the TPD temperatures for LaBO_3 (B=Mn, Fe, Co, and Ni) surface lattice oxygen desorption. In the following discussion we focus on the reaction energetics from the optimal U_{eff} since these are expected to be the most accurate.

The absence of a desorption peak for surface oxygens in $LaFeO_3$ up to 1100 K (Refs. 75 and 81) is fully consistent with the very high surface vacancy formation free energies predicted by the calculations. Similarly, the onset of the β-oxygen desorption temperature around 500 K in the $LaNiO_3$ TPD experiment[75] is consistent with the very low surface vacancy formation free energies for $LaNiO_3$. The ΔG^*_{vac} of $LaNiO_3$ shown in Fig. 12 is near zero even at 300 K, which is a somewhat lower value than measured experimentally. However, at such low temperature it is likely that the lattice oxygen desorption reaction is suppressed by kinetic barriers in the experiments, which could account for the higher measured temperature of desorption. It is also likely that the low $LaNiO_3$ surface ΔG^*_{vac} will result in understoichiometry for $LaNiO_3$ under SOFC conditions and therefore alter the reaction energetics by introducing doped electrons into the system. This will make it harder to form new vacan-

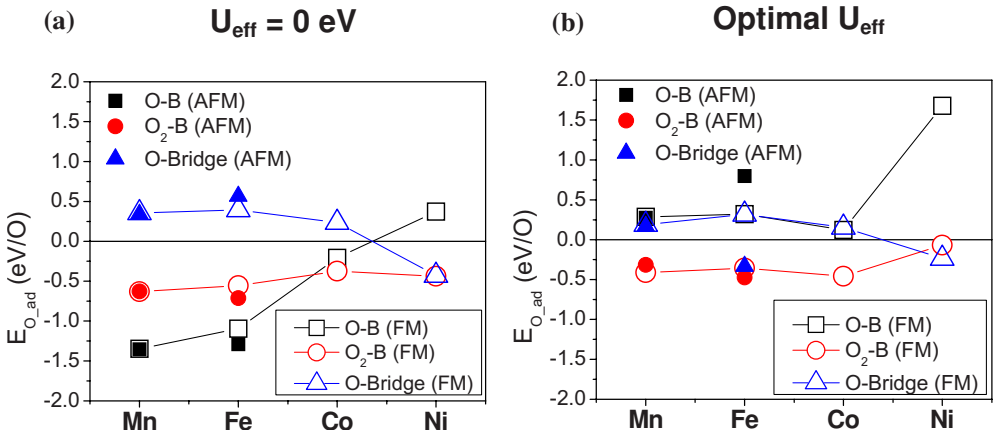

FIG. 13. (Color online) LaBO_3 BO_2 surface oxygen adsorption energies vs transition metal types (B=Mn, Fe, Co, and Ni) (a) at U_{eff} =0 eV and (b) at optimal U_{eff}.

cies and increase the temperature where surface oxygen desorption is observed. Finally, a shift in the $LaNiO_3$ vacancy formation energetics of about 0.2 eV is enough to move the zero crossing value in Fig. 12 up to about 500 K, which would agree well with the experiments. 0.2 eV is certainly within the errors of these calculations and may be the source of the discrepancy.

For $LaMnO_3$, an obvious β-oxygen desorption peak between 800 and 1100 K in O_2 TPD[75,81] suggests a much lower ΔG^*_{vac} than our calculated value (the intercept temperature at ΔG^*_{vac}=0 for $LaMnO_3$ at optimal U_{eff} is ~2400 K). The discrepancy is likely due to the $LaMnO_3$ oxygen overstoichiometry ($LaMnO_{3+\delta}$, where δ=0.08–0.18 between 873 and 1273K) in the high $P(O_2)$ region.[71,82] The overstoichiometry is due to cation vacancies, which introduce electron holes into the system. These extra holes can be thought of as creating Mn^{4+}, which will be easier to reduce than Mn^{3+} in the stoichiometric sample and will make it easier to form oxygen vacancies than our stoichiometric calculations suggest. In fact, it has been reported in Refs. 75 and 76 that thermoreduction temperature for $Mn^{4+} \rightarrow Mn^{3+}$ is 808 K, while that for $Mn^{3+} \rightarrow Mn^{2+}$ is 1353 K, consistent with significantly easier reduction energies for $Mn^{4+} \rightarrow Mn^{3+}$ compared to $Mn^{3+} \rightarrow Mn^{2+}$. Therefore, the desorption temperature of surface oxygen of overstoichiometirc $LaMnO_{3+\delta}$ under SOFC conditions is expected to be strongly overestimated by using the stoichiometric $LaMnO_3$ surface ΔG^*_{vac}, which is consistent with our results. It is worth noting that the ΔG^*_{vac} predicted for U_{eff}=0 is clearly much too large, further supporting the need to use optimal U_{eff}.

Similarly to $LaMnO_3$, the predicted ΔG^*_{vac} for $LaCoO_3$ seems at first inconsistent with the measured TPD peaks for surface oxygen. TPD experiments yield a $LaCoO_3$ surface oxygen desorption peak between 1000 and 1100 K.[75,78] Our predicted temperature for surface oxygen desorption based on where ΔG^*_{vac} crossed zero is about 630 K at $P(O_2)$ =0.2 atm and would drop even further at the lower PO_2 used in the TPD experiments (a flow of high purity helium carrier gas is generally applied during the O_2 TPD measurements[78,81]). Besides kinetic factors, which could cause a temperature hysteresis on the appearance of the lattice oxygen desorption during the heating of the TPD, we believe that the source of the discrepancy, as with $LaMnO_3$, is that the *ab initio* calculations are for a stoichiometric materials while the real material under experimental conditions will likely be nonstoichiometric. As mentioned previously, it has been reported in Ref. 77 that an almost linear decrease in the oxygen chemical potential is found with increasing net electron concentration for $La_{1-x}Sr_xCoO_{3-\delta}$. The calculated oxygen vacancy formation energies are therefore expected to be dependent on the change of the Fermi energy level from electron or hole doping. For a system at low PO_2 with significant oxygen vacancies we expect that the desorption of surface oxygen will occur at a higher temperature than that predicted by stoichiometric compound energetics. The nonstoichiometry effect upon reaction energetics of LaBO_3 systems is currently under further investigation.

2. Oxygen adsorption energies vs B

Figure 13 shows the *ab initio* calculated oxygen adsorption energetics for each metal cation for both U_{eff}=0 eV [Fig. 13(a)] and U_{eff}=optimal [Fig. 13(b)]. The O adsorption energetics at optimal U_{eff} suggest that O_2-B adsorption is more stable than the O-B adsorption for all the four LaBO_3 systems, in contrast to the O adsorption energetics at U_{eff} =0 eV, which suggest that O-B adsorption is energetically more favorable than O_2-B adsorption for $LaMnO_3$ and $LaFeO_3$. The change with U_{eff} is consistent with the general trend of increasing redox potential with U_{eff}. Since DFT+U stabilizes the reduction products and destabilizes the oxidation products, the O-B adsorption, in which oxygen adatom is doubly bonded to the surface B cation (strong oxidation of B), will be destabilized with increasing U_{eff}.

Here we compare the *ab initio* predictions to experimental data on surface oxygen species in LaBO_3 and closely related compounds. The chemisorbed diatomic oxygen species on LaBO_3 or Sr doped LaBO_3 surfaces are commonly reported as α oxygens in experiments[78,80,81,83,84] and they are identified with a desorption peak existing at a lower temperature as compared to that of structural β oxygens. The amounts of desorbed α oxygens and the α oxygen desorption temperature tend to decrease with the increase of atomic number of the transition metal with the exception of $LaFeO_3$ [$LaFeO_3$ has the lowest α-oxygen adsorption capacity among the ex-

plored B's (B=Cr, Mn, Fe, Co, and Ni) in the TPD experiments[81] and exhibits no α-oxygen desorption peak during the heating to 1073 K]. Except for $LaFeO_3$, it is shown in Ref. 81 that α oxygens on $LaBO_3$ surfaces are desorbed upon heating between 473 and 673 K. In Ref. 83, two chemisorbed dioxygens (O_2^- and O_2^{2-}) on $La_{0.8}Sr_{0.2}MnO_3$ were observed by diffuse reflectance Fourier transformed infrared spectrometry in the temperature range of 773–873 K and such dioxygen species are desorbed above 873 K. The above experimental observations suggest that the binding of adsorbed α oxygens on LaBO_3 surfaces could be weak since the α-oxygen desorption peaks occur at relatively low temperatures. The low-temperature desorption is generally consistent with the weak binding energies (<0.5 eV) found for the optimal U_{eff} in Fig. 13(b) [and inconsistent with the very strong binding energies for some cases found with U_{eff}=0 in Fig. 13(a)]. In addition, the spectrometry suggests that adsorbed dioxygen species (O_2-B or O-bridge), instead of dissociatively adsorbed and doubly bonded O-B monomers, are the more stable oxygen species on $LaMnO_3$ surfaces at lower temperatures.[81,83,84] This is again broadly consistent with the adsorption energetics for optimal U_{eff}, which suggests that dioxygen species are the most stable on the surface. However, the adsorption energies at the optimal U_{eff} suggest that the amount of O-bridge (O_2^{2-}) adsorption under equilibrium conditions is much smaller than the O_2-B (O_2^-) adsorption at low temperatures (except for $LaNiO_3$) on (001) BO_2 surfaces. It is possible that other factors not treated in our calculations, such as the existence of other types of surfaces or the insulator or semiconductor and magnetic characteristics at low temperature, could result in the greater amount of surface O_2^{2-} peroxides in the experiments. More extensive calculations and detailed experiments will be needed to make a more precise comparison. Here we simply point out the qualitative agreement between the experimental results (the weak LaBO_3 oxygen adsorption energy and the observation of surface adsorbed dioxygen species instead of doubly bonded oxygen and atom) and the calculated oxygen adsorption energetics at the optimal U_{eff}.

In order to consider the effects of temperature on the oxygen adsorption, Figs. 14(a)–14(c) show the ΔG^* of surface O-B, O-bridge, and O_2-B adsorptions on $LaFeO_3$ FM, $LaFeO_3$ GAFM, and $LaCoO_3$ FM BO_2 surfaces, respectively. $LaFeO_3$ and $LaCoO_3$ are chosen as they do not exhibit as significant oxygen nonstoichiometry[73,74] as $LaMnO_3$ and $LaNiO_3$ under SOFC conditions, so we expect our stoichiometric LaBO_3 DFT simulations to be the most accurate for these two systems. The surface adsorption free energies, ΔG^*_{ad}, are normalized per B site so that the ΔG^*_{ad} of the surface O_2-B adsorption is equal to $2\Delta G^*_{O_2\text{-}B}$, that of the surface O-$B$ adsorption is equal to $\Delta G^*_{O\text{-}B}$, and that of the surface O-bridge adsorption is equal to $\Delta G^*_{\text{O-bridge}}$. The motivation for this normalization is that, assuming only one O-bridge can be absorbed near each B site (each B site is surrounded by four bridge sites), ΔG^*_{ad} is easier to relate to concentration, measured as a fraction of B sites occupied. Figures 15(a)–15(c) show the corresponding B-site coverage vs temperature using the ideal Langmuir adsorption model[85] with the calculated oxygen adsorption ΔG^*_{ad}. It is seen that

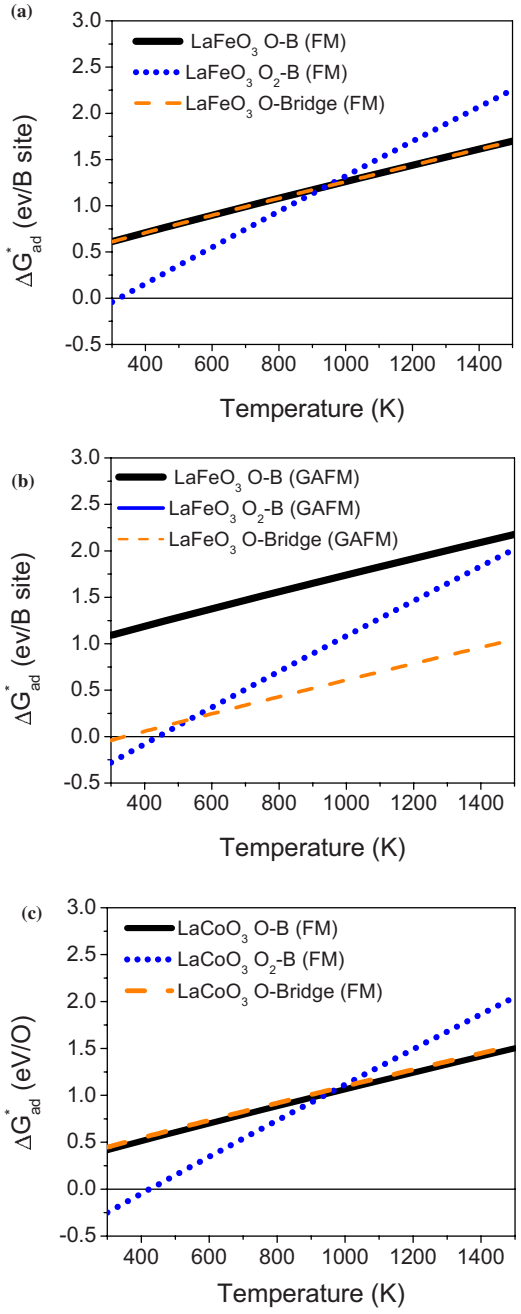

FIG. 14. (Color online) ΔG^*_{ad} (per B site) vs temperature (O-B: solid black line, O_2-B: dotted blue line, and O-bridge: dashed orange line at $P(O_2)$=0.2 atm at the optimal U_{eff} for (a) $LaFeO_3$ (FM), (b) $LaFeO_3$ (GAFM), and (b) $LaCoO_3$ (FM) BO_2 surfaces.

adsorbed O_2 dimers are the most stable surface oxygen species on the $LaFeO_3$ and $LaCoO_3$ surfaces at lower temperatures. Due to large entropy contributions in the O_2 gas phase, all the oxygen surface species are destabilized with increasing temperature. The positive ΔG^*_{ad} at high temperatures suggest a very low oxygen surface coverage under SOFC conditions. Since O_2-B has twice as much O adsorption per B site as compared to O-B and O-bridge adsorptions, the slope of O_2-B ΔG^*_{ad} vs T is almost twice (not exact twice because of different vibrational free energy treatments for adsorbed O_2 dimer and O monomer) that of O-B and O-bridge. These

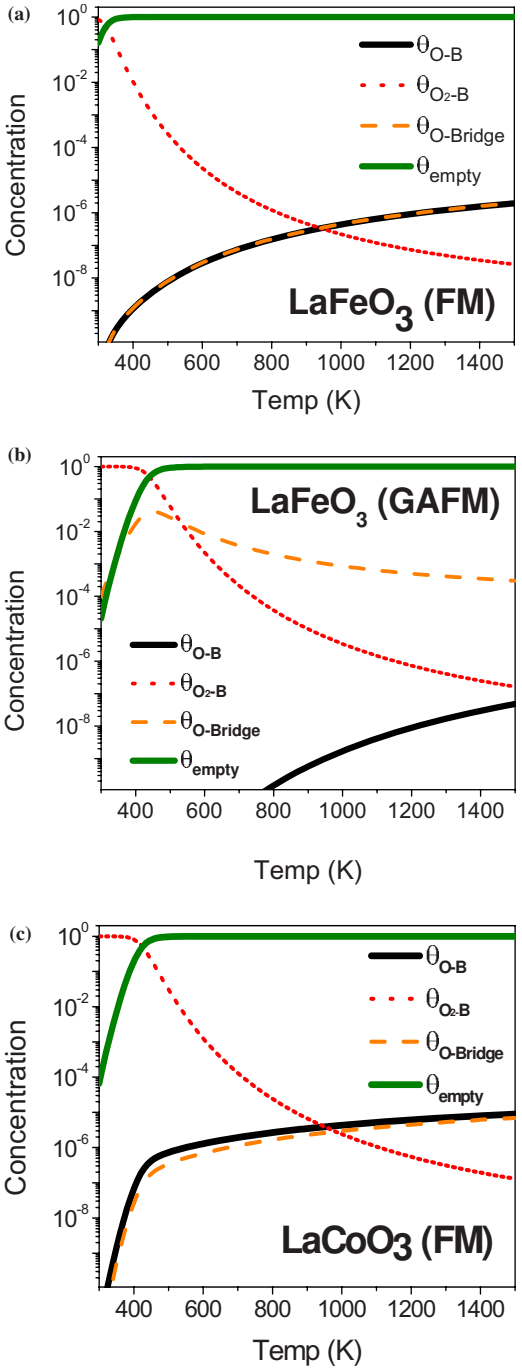

FIG. 15. (Color online) Surface *B*-site coverage based on the ideal Langmuir adsorption model with the calculated $\Delta G^{*}_{\mathrm{O\_ad}}$ [$P(\mathrm{O_2})=0.2$ atm] at the optimal U_{eff} for (a) $LaFeO_3$ (FM), (b)$LaFeO_3$ (GAFM), and (c) $LaCoO_3$. The results suggest that BO_2 surface *B* sites are likely to be covered by adsorbed O_2 dimers at low temperatures. The adsorbed O_2 dimmer would be desorbed upon heating and surface *B*-site coverage becomes small (almost bare surface).

slopes suggests that although O_2-*B* adsorption is more stable than O-*B* and O-bridge at low temperatures, a crossover of $\Delta G^{*}_{\mathrm{ad}}$ of O_2-*B* vs O-*B* (and O-bridge) would eventually occur at a higher temperature. Above this crossover temperature, the adsorbed O monomer state would become more stable than the adsorbed O_2 dimer state. This transition to absorbed monomers is essentially due to the greater surface configurational entropy of the separate O compared to O_2 molecules. It is noted that the intrinsic *ab initio* and convergence errors (likely as large as a few hundred meV) in this work could result in significant deviation in the prediction of low-temperature coverage behavior in Fig. 15. Additional uncertainties in the analysis leading to Fig. 15 are introduced by the assumption of a Langmuir isotherm and ideal solution behavior for the oxygen species on the surface. Despite the many uncertainties in the calculations, they demonstrate the qualitative trends we expect with temperature and suggest that entropic effects and binding energies are close enough that an entropy driven crossover from dioxygen to monomer oxygen species is possible. Above the crossover temperature oxygen would largely dissociate on the surface (although kinetic barriers may inhibit the process) even without the aid of surface vacancies to split the oxygen.

It is important to note that the adsorption energetics shown in Fig. 14 were calculated for the stoichiometric system and will have similar limitations to those identified for stoichiometic vacancy energetics. In particular, under SOFC conditions, $LaMnO_3$ exhibits overstoichiometry ($LaMnO_{3+\delta}$) and $LaNiO_3$ exhibits understoichiometry ($LaNiO_{3-\delta}$). The surface oxygen adsorption energies involving oxidation of surface *B* cations (O-*B* and O_2-*B*) will be higher for $LaMnO_{3+\delta}$ and lower for $LaNiO_{3-\delta}$ when compared to the stoichiometric phases. Similar changes will occur for the $LaCoO_3$ and $LaFeO_3$ compounds, although we expect the deviations from stoichiometry to be smaller than for $LaMnO_3$ and $LaNiO_3$.

IV. SUMMARY

To investigate $LaBO_3$ (*B*=Mn, Fe, Co, and Ni) ORR energetics under SOFC conditions, we have applied GGA+*U* calculations with O_2 energy correction to account for the self-interaction errors in the $LaBO_3$ solids and the energy error from O_2 gas molecules entering into oxide solids in DFT. We have further combined the calculated *ab initio* reaction energies with an empirical oxygen chemical potential and vibrational free energy corrections to estimate the nonconfigurational contribution to defects and surface adsorption reaction free energies (ΔG^{*}) under SOFC conditions. Important surface properties related to the cathodic oxygen reduction reaction in SOFCs, such as surface oxygen vacancies and adsorbed surface oxygen species, are studied through the reaction energies of oxygen vacancy formation and adsorption (O-*B*, O_2-*B*, and O-bridge). All surface studies are focused on (001) BO_2 surfaces since it was determined that (001) LaO terminated surfaces, due to their high oxygen binding energies, were likely to be passivated and not play a major role in the oxygen reduction reaction (ORR). A wide range of U_{eff} (U_{eff}=0–6.4 eV) are explored to understand the reaction energies vs U_{eff} trends. It is seen that the reaction energies associated with reduction reactions are generally decreased and those associated with oxidation reaction are increased with increasing U_{eff}, and the extent of reaction energy dependence on U_{eff} is correlated with the

extent of reduction or oxidation in the reaction. An exception to this trend with U_{eff} is bulk $LaFeO_3$, where an increase of oxygen vacancy formation energy upon increasing U_{eff} is found. This exception is shown to arise because of the unique electronic structure of $LaFeO_3$, which has a half filled *d* shell. Surprisingly, this exception for bulk $LaFeO_3$ does not occur at the surface. Due to surface effects, surface Fe^{3+} ions are partially oxidized and do not have the half filled *d* shell seen in the bulk. The surface vacancy formation reaction energies therefore do not exhibit the same trends with U_{eff} as the $LaFeO_3$ bulk.

We have applied the optimal U_{eff} from Ref. 25 to investigate the reaction energetics vs transition metal types. Our optimal U_{eff} results suggest that the order of LaBO_3 oxygen vacancy formation energies is Fe > Mn > Co > Ni. The calculations predict that O_2-*B* adsorption (O-bridge for Ni) is the more stable oxygen species than O-*B* at low temperatures and that oxygen coverage on these systems is likely to be very low under operating conditions. The results for oxygen vacancies and adsorption are in better agreements with experimental data (both oxygen vacancy formation enthalpies and oxygen desorption in O_2 TPD experiments) than those at $U_{\text{eff}}=0$ eV. The results suggest that defect reaction energy errors are quite significant with pure LDA/GGA and can be reduced by applying U_{eff}. It is possible that kinetic barriers will also exhibit U_{eff} dependence since transition states of reactions can involve at least partial oxidation or reduction of the systems.

We have shown that (001) BO_2 surface E_{vac} are 1–2 eV lower than those of the bulk for all the four LaBO_3 systems and across all U_{eff}. Although it is expected that surface oxygen vacancy concentration is higher than in the bulk, our calculation results demonstrate a very large quantitative effect. This suggests that for systems with high bulk E_{vac} such as $LaMnO_3$ and $LaFeO_3$, the surface vacancy concentration will be orders of magnitude larger than in the bulk, which will impact the surface vs bulk oxygen transport and other surface processes associated with the ORR. For systems with low bulk E_{vac}, such as $LaCoO_3$ and $LaNiO_3$, although their surface vacancy concentrations are also expected to be higher than their bulk values, the larger bulk concentrations cannot be amplified by nearly as large a factor before defect interactions start to change the energetics. The energetics calculated in this paper can be used to help build models of important surface properties related to the ORR, e.g., surface oxygen vacancy concentration, surface oxygen diffusion coefficient, and surface oxygen exchange coefficient. The results provided here help in understanding the surfaces of LaBO_3 (*B*=Mn, Fe, Co, Ni) perovskites and are a valuable foundation for performing studies of ORR mechanisms.

ACKNOWLEDGMENTS

We gratefully acknowledge financial support from NSF MRSEC program (Grant No. 0079983) and computing support from NSF National Center for Supercomputing Applications (Grant No. NCSA-DMR060007).

[1] S. B. Adler, Chem. Rev. (Washington, D.C.) **104**, 4791 (2004).
[2] S. C. Singhal and K. Kendall, *High-Temperature Solid Oxide Fuel Cells: Fundamentals, Design and Applications*, 1st ed. (Elsevier Science, New York, 2004).
[3] J. K. Nørskov, M. Scheffler, and H. Toulhoat, MRS Bull. **31**, 669 (2006).
[4] V. I. Anisimov, F. Aryasetiawan, and A. I. Lichtenstein, J. Phys.: Condens. Matter **9**, 767 (1997).
[5] G. Pacchioni, J. Chem. Phys. **128**, 182505 (2008).
[6] V. I. Anisimov, J. Zaanen, and O. K. Andersen, Phys. Rev. B **44**, 943 (1991).
[7] I. Solovyev, N. Hamada, and K. Terakura, Phys. Rev. B **53**, 7158 (1996).
[8] Z. Q. Yang, Z. Huang, L. Ye, and X. D. Xie, Phys. Rev. B **60**, 15674 (1999).
[9] H. Sawada, Y. Morikawa, K. Terakura, and N. Hamada, Phys. Rev. B **56**, 12154 (1997).
[10] M. A. Korotin, S. Y. Ezhov, I. V. Solovyev, V. I. Anisimov, D. I. Khomskii, and G. A. Sawatzky, Phys. Rev. B **54**, 5309 (1996).
[11] I. R. Shein, K. I. Shein, V. L. Kozhevnikov, and A. L. Ivanovskii, Phys. Solid State **47**, 2082 (2005).
[12] G. Trimarchi and N. Binggeli, Phys. Rev. B **71**, 035101 (2005).
[13] S. K. Pandey, S. Khalid, and A. V. Pimpale, J. Phys.: Condens. Matter **19**, 036212 (2007).
[14] S. K. Pandey, A. Kumar, S. Patil, V. R. R. Medicherla, R. S. Singh, K. Maiti, D. Prabhakaran, A. T. Boothroyd, and A. V. Pimpale, Phys. Rev. B **77**, 045123 (2008).
[15] E. A. Kotomin, Y. A. Mastrikov, E. Heifets, and J. Maier, Phys. Chem. Chem. Phys. **10**, 4644 (2008).
[16] Y. M. Choi, D. S. Mebane, M. C. Lin, and M. L. Liu, Chem. Mater. **19**, 1690 (2007).
[17] R. A. Evarestov, E. A. Kotomin, Y. A. Mastrikov, D. Gryaznov, E. Heifets, and J. Maier, Phys. Rev. B **72**, 214411 (2005).
[18] Y. Choi, M. C. Lin, and M. L. Liu, Angew. Chem., Int. Ed. **46**, 7214 (2007).
[19] A. Rohrbach, J. Hafner, and G. Kresse, Phys. Rev. B **69**, 075413 (2004).
[20] A. Rohrbach and J. Hafner, Phys. Rev. B **71**, 045405 (2005).
[21] S. Piskunov, E. Heifets, T. Jacob, E. A. Kotomin, D. E. Ellis, and E. Spohr, Phys. Rev. B **78**, 121406(R) (2008).
[22] T. Ohnishi, K. Takahashi, M. Nakamura, M. Kawasaki, M. Yoshimoto, and H. Koinuma, Appl. Phys. Lett. **74**, 2531 (1999).
[23] M. M. Viitanen, R. G. von Welzenis, H. H. Brongersma, and F. P. F. van Berkel, Solid State Ionics **150**, 223 (2002).
[24] Y. F. Zhukovskii, E. A. Kotomin, R. A. Evarestov, and D. E. Ellis, Int. J. Quantum Chem. **107**, 2956 (2007).
[25] L. Wang, T. Maxisch, and G. Ceder, Phys. Rev. B **73**, 195107 (2006).
[26] G. Kresse and J. Furthmuller, Phys. Rev. B **54**, 11169 (1996).
[27] J. P. Perdew, K. Burke, and M. Ernzerhof, Phys. Rev. Lett. **77**, 3865 (1996).
[28] G. Kresse and D. Joubert, Phys. Rev. B **59**, 1758 (1999).

[29] H. J. Monkhorst and J. D. Pack, Phys. Rev. B **13**, 5188 (1976).
[30] A. I. Liechtenstein, V. I. Anisimov, and J. Zaanen, Phys. Rev. B **52**, R5467 (1995).
[31] S. L. Dudarev, G. A. Botton, S. Y. Savrasov, C. J. Humphreys, and A. P. Sutton, Phys. Rev. B **57**, 1505 (1998).
[32] J. S. Zhou and J. B. Goodenough, Phys. Rev. B **60**, R15002 (1999).
[33] C. Zobel, M. Kriener, D. Bruns, J. Baier, M. Gruninger, T. Lorenz, P. Reutler, and A. Revcolevschi, Phys. Rev. B **66**, 020402(R) (2002).
[34] M. C. Sanchez, G. Subias, J. Garcia, and J. Blasco, Phys. Rev. Lett. **90**, 045503 (2003).
[35] C. A. Marianetti, D. Morgan, and G. Ceder, Phys. Rev. B **63**, 224304 (2001).
[36] D. Treves, M. Eibschütz, and P. Coppens, Phys. Lett. **18**, 216 (1965).
[37] J. B. Goodenough and P. M. Raccah, J. Appl. Phys. **36**, 1031 (1965).
[38] F. Zhou, M. Cococcioni, C. A. Marianetti, D. Morgan, and G. Ceder, Phys. Rev. B **70**, 235121 (2004).
[39] M. W. Chase, *NIST-JANAF Thermochemical Tables* (American Chemical Society, New York, 1998).
[40] O. Kubaschewski, C. B. Alcock, and P. I. Spencer, *Materials Thermochemistry* (Pergamon Press, Oxford, 1993).
[41] J. A. Pople, M. Headgordon, D. J. Fox, K. Raghavachari, and L. A. Curtiss, J. Chem. Phys. **90**, 5622 (1989).
[42] C. Laberty, A. Navrotsky, C. N. R. Rao, and P. Alphonse, J. Solid State Chem. **145**, 77 (1999).
[43] J. H. Cheng, A. Navrotsky, X. D. Zhou, and H. U. Anderson, J. Mater. Res. **20**, 191 (2005).
[44] A. F. Wells, *Structural Inorganic Chemistry* (Clarendon Press, Oxford, 1984).
[45] E. A. Kotomin, E. Heifets, S. Dorfman, D. Fuks, A. Gordon, and J. Maier, Surf. Sci. **566-568**, 231 (2004).
[46] J. Neugebauer and M. Scheffler, Phys. Rev. B **46**, 16067 (1992).
[47] G. Makov and M. C. Payne, Phys. Rev. B **51**, 4014 (1995).
[48] K. Reuter and M. Scheffler, Phys. Rev. B **65**, 035406 (2001).
[49] K. Johnston, M. R. Castell, A. T. Paxton, and M. W. Finnis, Phys. Rev. B **70**, 085415 (2004).
[50] E. Heifets, J. Ho, and B. Merinov, Phys. Rev. B **75**, 155431 (2007).
[51] Y. A. Mastrikov, E. Heifets, E. A. Kotomin, and J. Maier, Surf. Sci. **603**, 326 (2009).
[52] NIST, in *NIST Chemistry WebBook*, NIST Standard Reference Database No. 69, edited by P. J. Linstrom and W. G. Mallard (National Institute of Standards and Technology, Gaithersburg, MD, 2003), http://webbook.nist.gov/chemistry/
[53] J. Callaway, *Quantum Theory of the Solid State* (Academic Press, New York, 1974).
[54] G. Herzberg, *Molecular Spectra and Molecular Structure, I. Spectra of Diatomic Molecules*, 2nd ed. (Van Nostrand, Princeton, NJ, 1950).
[55] R. F. W. Bader, *Atoms in Molecules: A Quantum Theory* (Clarendon Press, Oxford, 1994).
[56] G. Henkelman, A. Arnaldsson, and H. Jonsson, Comput. Mater. Sci. **36**, 354 (2006).
[57] J. Rodriguez-Carvajal, M. Hennion, F. Moussa, A. H. Moudden, L. Pinsard, and A. Revcolevschi, Phys. Rev. B **57**, R3189 (1998).
[58] H. Falcon, A. E. Goeta, G. Punte, and R. E. Carbonio, J. Solid State Chem. **133**, 379 (1997).
[59] P. M. Raccah and J. B. Goodenough, Phys. Rev. **155**, 932 (1967).
[60] K. Huang, H. Y. Lee, and J. B. Goodenough, J. Electrochem. Soc. **145**, 3220 (1998).
[61] M. A. Señarís-Rodríguez and J. B. Goodenough, J. Solid State Chem. **116**, 224 (1995).
[62] E. Heifets, R. A. Evarestov, E. A. Kotomin, S. Dorfman, and J. Maier, Sens. Actuators B **100**, 81 (2004).
[63] T. Arima, Y. Tokura, and J. B. Torrance, Phys. Rev. B **48**, 17006 (1993).
[64] K. Tobe, T. Kimura, Y. Okimoto, and Y. Tokura, Phys. Rev. B **64**, 184421 (2001).
[65] N. N. Kovaleva, A. V. Boris, C. Bernhard, A. Kulakov, A. Pimenov, A. M. Balbashov, G. Khaliullin, and B. Keimer, Phys. Rev. Lett. **93**, 147204 (2004).
[66] J. Q. Yan, J. S. Zhou, and J. B. Goodenough, Phys. Rev. B **70**, 014402 (2004).
[67] A. Rohrbach, J. Hafner, and G. Kresse, Phys. Rev. B **70**, 125426 (2004).
[68] M. Cococcioni and S. de Gironcoli, Phys. Rev. B **71**, 035105 (2005).
[69] J. K. Nørskov, T. Bligaard, A. Logadottir, S. Bahn, L. B. Hansen, M. Bollinger, H. Bengaard, B. Hammer, Z. Sljivancanin, M. Mavrikakis, Y. Xu, S. Dahl, and C. J. H. Jacobsen, J. Catal. **209**, 275 (2002).
[70] C. Loschen, S. T. Bromley, K. M. Neyman, and F. Illas, J. Phys. Chem. C **111**, 10142 (2007).
[71] J. H. Kuo, H. U. Anderson, and D. M. Sparlin, J. Solid State Chem. **83**, 52 (1989).
[72] J. Nowotny and M. Rekas, J. Am. Ceram. Soc. **81**, 67 (1998).
[73] J. Mizusaki, M. Yoshihiro, S. Yamauchi, and K. Fueki, J. Solid State Chem. **58**, 257 (1985).
[74] J. Mizusaki, Y. Mima, S. Yamauchi, K. Fueki, and H. Tagawa, J. Solid State Chem. **80**, 102 (1989).
[75] Y. Teraoka, M. Yoshimatsu, N. Yamazoe, and T. Seiyama, Chem. Lett. **13**, 893 (1984).
[76] *Mukikagaku Handbook* (Gihodo Shuppan, Tokyo, 1981).
[77] M. H. R. Lankhorst, H. J. M. Bouwmeester, and H. Verweij, Phys. Rev. Lett. **77**, 2989 (1996).
[78] N. Yamazoe, Y. Teraoka, and T. Seiyama, Chem. Lett. **10**, 1767 (1981).
[79] S. Royer, D. Duprez, and S. Kaliaguine, Catal. Today **112**, 99 (2006).
[80] M. A. Peña and J. L. G. Fierro, Chem. Rev. (Washington, D.C.) **101**, 1981 (2001).
[81] Y. Yokoi and H. Uchida, Catal. Today **42**, 167 (1998).
[82] J. Mizusaki, N. Mori, H. Takai, Y. Yonemura, H. Minamiue, H. Tagawa, M. Dokiya, H. Inaba, K. Naraya, T. Sasamoto, and T. Hashimoto, Solid State Ionics **129**, 163 (2000).
[83] N. Caillol, M. Pijolat, and E. Siebert, Appl. Surf. Sci. **253**, 4641 (2007).
[84] M. Imamura, N. Matsubayashi, and H. Shimada, J. Phys. Chem. B **104**, 7348 (2000).
[85] C. H. P. Lupis, *Chemical Thermodynamics of Materials* (North-Holland, New York, 1983).